EVALUATION OF ROTATIONAL MECHANISMS TO ENHANCE PERFORMANCE OF A RESPIRATORY ASSIST CATHETER

by

Kevin Michael Mihelc

B.S. in Bioengineering, University of Pittsburgh, 2005

Submitted to the Graduate Faculty of

the School of Engineering in partial fulfillment

of the requirements for the degree of

Master of Science in Bioengineering

University of Pittsburgh

2007

UNIVERSITY OF PITTSBURGH

SCHOOL OF ENGINEERING

This thesis was presented

by

Kevin Michael Mihelc

It was defended on

May 11, 2007

and approved by

Brack G. Hattler, M.D., Ph.D.

Professor, Department of Surgery

Harvey S. Borovetz, Ph.D.

Professor and Chair, Departments of Bioengineering, Surgery, and Chemical Engineering

Thesis Advisor: William J. Federspiel, Ph.D.

Professor, Departments of Chemical Engineering, Bioengineering, and Surgery

EVALUATION OF ROTATIONAL MECHANISMS TO ENHANCE PERFORMANCE OF A RESPIRATORY ASSIST CATHETER

Kevin Michael Mihelc, M.S.

University of Pittsburgh, 2007

A percutaneous respiratory assist catheter is being developed to partially support native lung function in patients with acute respiratory distress syndrome (ARDS) and acute exacerbations of chronic obstructive pulmonary disease (COPD). Current clinical therapies include pharmacotherapy, mechanical ventilation, and ECLS, but are associated with high mortality rates. The catheter is intended for insertion through the femoral vein for placement in the vena cava where it actively processes venous blood. The artificial lung device consists of a hollow fiber membrane (HFM) bundle that supplements oxygenation and carbon dioxide removal through diffusional processes.

The catheter is a second generation concept of the Hattler Catheter with a design goal of size reduction to accommodate percutaneous insertion. The tradeoff in available HFM surface area requires the catheter to be more efficient in removing CO_2 per unit surface area. Two prototypes utilizing rotational mechanisms to actively mix the blood and reduce mass transfer boundary layers were evaluated. The first prototype consisted of a rotating HFM bundle capable of rates of 10,000 RPM but required a structure for vessel wall protection. The second prototype employed a rotating impeller within a stationary HFM bundle to internalize rotational components within the device.

The prototypes were evaluated *in vitro* and *in vivo* to assess design and performance. Development of impeller geometries, a saline seal purge, and device flexibility were notable

design highlights. Acceptable hemolysis levels were observed in testing the concept of using a high-speed rotational HFM bundle. Standard gas exchange characterization tests in DI water showed over a two-fold increase in CO_2 removal efficiency of 450 and 529 ml CO_2/min/m^2, rotational catheter and impeller catheter respectively, over the Hattler Catheter. The impeller catheter was evaluated in a bovine model and an average efficiency of 513 ± 20 ml CO_2/min/m^2 was attained at 20,000 RPM. Catheter size reduction and CO_2 removal efficiency enhancements were successfully achieved. A separate novel method to augment CO_2 concentration gradients is being researched to integrate with HFMs and attain overall gas exchange project goals.

TABLE OF CONTENTS

PREFACE ..... **xi**

1.0 BACKGROUND **1**

1.1 INTRODUCTION **1**

1.2 CURRENT CLINICAL THERAPIES **2**

1.3 PRINCIPLES OF HOLLOW FIBER MEMBRANE GAS EXCHANGE **6**

1.4 INTRAVASCULAR RESPIRATORY SUPPORT THERAPY **9**

1.5 PERCUTANEOUS RESPIRATORY ASSIST CATHETER **15**

2.0 ROTATING FIBER BUNDLE CATHETER **19**

2.1 DESIGN AND FABRICATION **21**

2.1.1 Prototype Designs **21**

2.1.2 Fabrication **27**

2.2 EVALUATIVE TESTS **29**

2.2.1 Gas Exchange **30**

2.2.2 Hemolysis **33**

2.2.3 Safety Cage and Implantable Prototype **36**

2.3 RESULTS AND DISCUSSION **38**

2.3.1 Gas Exchange **38**

2.3.2 Hemolysis **42**

2.3.3 Safety Cage and Implantable Prototype 44
2.4 CONCLUSIONS 46
3.0 INTERNAL IMPELLER CATHETER 48
3.1 DESIGN AND FABRICATION 49
3.1.1 Prototype Designs 50
3.1.2 Fabrication 55
3.2 EVALUATIVE TESTS 56
3.2.1 Gas Exchange 56
3.2.2 Impeller Fatigue 57
3.2.3 Acute Animal Studies 59
3.3 RESULTS AND DISCUSSION 61
3.3.1 Gas Exchange 61
3.3.2 Impeller Fatigue 65
3.3.3 Acute Animal Studies 66
3.4 CONCLUSIONS 72
4.0 ROTATIONAL ENHANCEMENT CONCLUSIONS 73
APPENDIX A 76
APPENDIX B 81
APPENDIX C 84
BIBLIOGRAPHY 87

LIST OF TABLES

Table 2-1: HFMs (left) and rotational bundle (right) characteristics. 22

Table 2-2: New England Wire Technologies tubing. 27

Table 2-3: *In vitro* gas exchange test equipment. 32

Table 2-4: Hemolysis test equipment. 35

Table 2-5: Hemolysis results[44]. 42

Table 3-1: HFMs (left) and impeller bundle (right) characteristics. 50

Table 3-2: Fatigue test equipment. 59

Table 3-3: Maximum CO_2 removal efficiency corresponding to impeller geometry. 62

Table 4-1: Catheter performances. 74

Table A-1: Selected tubings for tortuous testing. 77

LIST OF FIGURES

Figure 1-1: Membrane oxygenator. 5

Figure 1-2: Porous wall structure of HFM (left), Bundle of HFMs (right). 7

Figure 1-3: Blood-side CO_2 diffusion into the lumen of a hollow fiber membrane. 8

Figure 1-4: Schematic of intravascular artificial lung implant. 9

Figure 1-5: Hattler Catheter. 12

Figure 2-1: Rotational bundle catheter concept. 20

Figure 2-2: Chicago Rawhide nitrile seal (left), Bal teflon seal (right). 23

Figure 2-3: Servomotor controller. 24

Figure 2-4: RPI-1 nitinol weave safety cage. 25

Figure 2-5: Micro-bubbles expelled from a rotating HFM bundle. 30

Figure 2-6: *In vitro* gas exchange schematic [44]. 31

Figure 2-7: Hemolysis circuit schematic. 35

Figure 2-8: Dimensions of the tortuous test section. 37

Figure 2-9: RP VCO_2 as a function of RPM [44]. 39

Figure 2-10: Micro-bubble influence on RP VCO_2 and design countermeasure. 41

Figure 2-11: Thrombus disparity between RP seals. 43

Figure 2-12: Prototype configuration in bovine vessel. 44

Figure 2-13: Displacement of safety cage resulting in critically damaged HFM bundle. 45

Figure 3-1: Internal impeller catheter concept. 49

Figure 3-2: Impeller catheter medial manifold (top) and distal manifold (bottom). 52

Figure 3-3: Impeller unit geometries. 53

Figure 3-4: Torsion testing apparatus. 55

Figure 3-5: Saline purge fatigue test circuit. 58

Figure 3-6: CO_2 removal efficiency plots according to impeller geometry 62

Figure 3-7: Impeller efficiency mass transfer correlation. 64

Figure 3-8: Effectiveness of saline purge in preventing impeller failure. 65

Figure 3-9: (Left) Seal thrombus observed in device without saline purge 66

Figure 3-10: (A) & (B): Tubing failures due to excessive torsion. 67

Figure 3-11: (A) Thrombus deposition on seal. (B) External bearing region. 68

Figure 3-12: IP-2 average maximum efficiencies observed *in vivo*. 69

Figure 3-13: *In vivo* IP-2 efficiency plot. 70

Figure 3-14: *In vivo* hemolysis generation for two impellers. 71

Figure A-1: Fluid viscosity influence on required motor torque. 78

Figure A-2: (A) Tortuous test section. (B) Tubing break with 1" impeller units. 79

Figure A-3: Torque levels of tubing samples in tortuous configuration. 80

Figure B-1: Concentric rotating cylinders. 81

Figure B-2: Impeller catheter external bearing schematic. 83

Figure C-1: IP-2 hemolysis generation in all animal implant studies. 86

PREFACE

I would like to thank my thesis advisor Dr. William Federspiel for his mentorship during my Master of Science studies in the Medical Devices Laboratory. Through his guidance I have greatly expanded my engineering skills and have acquired new abilities and approaches to solve challenging problems. The chance to work on a design project of medical devices with engineering issues spanning multiple disciplines has greatly prepared me for my future career. This project was a highly educational, developmental and exciting experience, and I appreciated the opportunity to work under his direction.

I would also like to thank my committee members Dr. Harvey Borovetz and Dr. Brack Hattler. I am very fortunate to have had their professional expertise of artificial organs and oxygenators in advising and providing feedback to improve my project.

I want to express gratitude to the wonderful personnel of the Medical Devices Laboratory. The personal and technical support was instrumental in making my years in graduate school a success. Best of luck to you all in your future endeavors.

Last but certainly not least, I want to thank my parents, brother and girlfriend for their continued encouragement. Knowing you are behind me through life's journey is invaluable and my appreciation far extends this acknowledgment.

This work was funded by the National Institutes of Health (NIH), National Heart, Lung, and Blood Institute (NHLBI) Grant Number HL70051.

1.0 BACKGROUND

1.1 INTRODUCTION

Lung disease remains one of the major healthcare problems present in the United States today. The American Lung Association states that lung disease is responsible for 1 in every 7 deaths, designating the disease as the number three killer amongst the American population[1]. Two significant contributors to lung disease are acute respiratory distress syndrome (ARDS), and chronic obstructive pulmonary disease (COPD). The National Heart, Lung, and Blood Institute suggests ARDS afflicts approximately 150,000 Americans yearly, while COPD affects an estimated 11.4 - 24 million adults[1]. COPD is listed as the fourth common cause of death and has a rate that continues to increase[2].

Acute respiratory distress syndrome is defined as a severe "syndrome of inflammation and increased permeability that is associated with a constellation of clinical, radiologic, and physiologic abnormalities that cannot be explained by, but may coexist with, left atrial or pulmonary capillary hypertension", according to the American-European Consensus Conference on ARDS in 1994[3]. It is a non-cardiogenic, acute respiratory complication characterized by a profound reduction in systemic oxygenation or ventilation, with an in-hospital mortality rate of 38.5%[4]. ARDS develops as a result of injury to the endothelium and epithelial layers of the alveolar membrane from stimuli such as sepsis, infection or trauma. The breakdown of the

capillary-alveolar barrier leads to alveolar flooding and an eventual deterioration of gas exchange capability[5].

In contrast to ARDS, chronic obstructive pulmonary disease is a persistent, irreversible condition that slowly progresses overtime. COPD refers to the existence or co-existence of chronic bronchitis and emphysema and is characterized by obstructed airways, enlarged air spaces and destruction of lung parenchyma, occlusion of small airways, and reduced lung elasticity[2]. When compared to normal, healthy lung function, patients with advanced stages of COPD can experience 10 to 20 times the work necessary to facilitate breathing[6]. Risk factors for COPD include smoking and exposure to air pollution such as chemicals, dust, and cooking smoke[2, 6]. The direct and indirect costs of COPD are staggering with an estimated $32.1 billion being spent in 2002. In 2000, approximately 119,000 people aged 25 or older died from COPD and it is projected to become the third leading cause of death in the U.S by the year 2020[7].

1.2 CURRENT CLINICAL THERAPIES

Hospital treatment for ARDS, acute exacerbations of COPD, and advanced COPD exist in three broad generalizations: pharmacological, mechanical ventilation and application of an extracorporeal membrane device (artificial lung). The treatment modalities depend on the severity of the disease as well as patient response to prior therapies. As indicated by the high mortality rates for the lung conditions, however, each therapy has associated limitations which can interrupt patient discharge from the hospital and/ or recovery. These therapies and limitations are discussed in further detail.

The least invasive and first line of defense in treating lung failure is to administer drugs that may improve the ailing condition. Multiple pharmacologic strategies have been investigated since the 1960's with therapies including prostaglandins, corticosteroids, nitric oxide, N-acetylcysteine, ketoconazole, and lisofylline. The purpose of most drugs are to ameliorate the inflammatory response in the lungs. Others such as nitric oxide and prostaglandins are vasodilators that can increase pulmonary circulation, and thus benefit overall gas exchange[4, 8]. Despite these therapeutic benefits, none of the investigated treatments have demonstrated an ability to improve patient survival[8, 9].

Mechanical ventilation is the most common therapy and serves to maintain respiratory function by rhythmically inducing a controlled flow of air into the lungs. In healthy persons, normal breathing consists of contracting the diaphragm to distend the lungs and create a negative pressure from atmosphere to lungs forcing fresh air in. Following oxygen and carbon dioxide gas exchange, the diaphragm relaxes compressing the lungs and forcing expiratory air to the external environment. Mechanical ventilation creates this effect but in an opposing manner; fresh air is driven into the lungs by positive pressure and expiratory air is pumped out of the lungs by a negative pressure.

Ventilators are operated in either of two principal modes: volume-controlled in which a predetermined tidal volume is delivered at a desired flowrate to the patient, or pressure-controlled in which flow is delivered over a given inspiratory time to meet a desired peak pressure. Respiratory function of a patient is regulated by altering the frequency, ratio of inspiration to expiration, and inspired gas oxygen tension[10]. These programmable variables are conducive to a number of more detailed ventilator modes monitoring levels of low tidal volume, positive end-expiratory pressure, and also high-frequency oscillatory ventilation. Clinical and

research studies using these methods have shown mixed results and an inability to considerably reduce mortality rates[4, 8, 10, 11].

Mechanical ventilation treatment is associated with multiple shortcomings termed ventilator-induced lung injury, or VILI. VILI covers a range of detrimental insults to the lung that can postpone recovery, cause unfavorable outcomes, or even intensify preexisting injury. Among these insults are volutauma, barotrauma, atelectrauma, biotrauma, and oxygen toxicity[4, 11]. Volutrauma is a result of excessive inspired volume that overdistends the alveoli and compromises the alveolar wall and vascular sheath junction, leading to inflammation and pulmonary edema[12]. Barotrauma injury derives from high airway pressures, which can promote air leakage and develop into pneumothorax and pneumomediastinum. The repetitive opening and closing of alveoli is classified as atelectrauma and produces harm from intolerable shear stresses[11]. Inflammation and increased biological mediators known as biotrauma are yet another form of injury with consequences of disease progression, multiple-organ dysfunction syndrome, and death[11, 13]. Finally, other complications can include weaning periods and oxygen toxicity due to the production of oxygen radicals from high O_2 content inspiratory gas.

The third clinical therapy being administered utilizes a membrane oxygenator and accompanying flow circuit. The treatment is denoted as extracorporeal membrane life support (ECLS) and Figure 1-1 displays a typical membrane oxygenator. The device processes patient blood by adding oxygen and removing carbon dioxide through fiber membrane technology discussed in section 1.3. It is essentially an artificial lung that replicates the gas exchange function of the natural lungs.

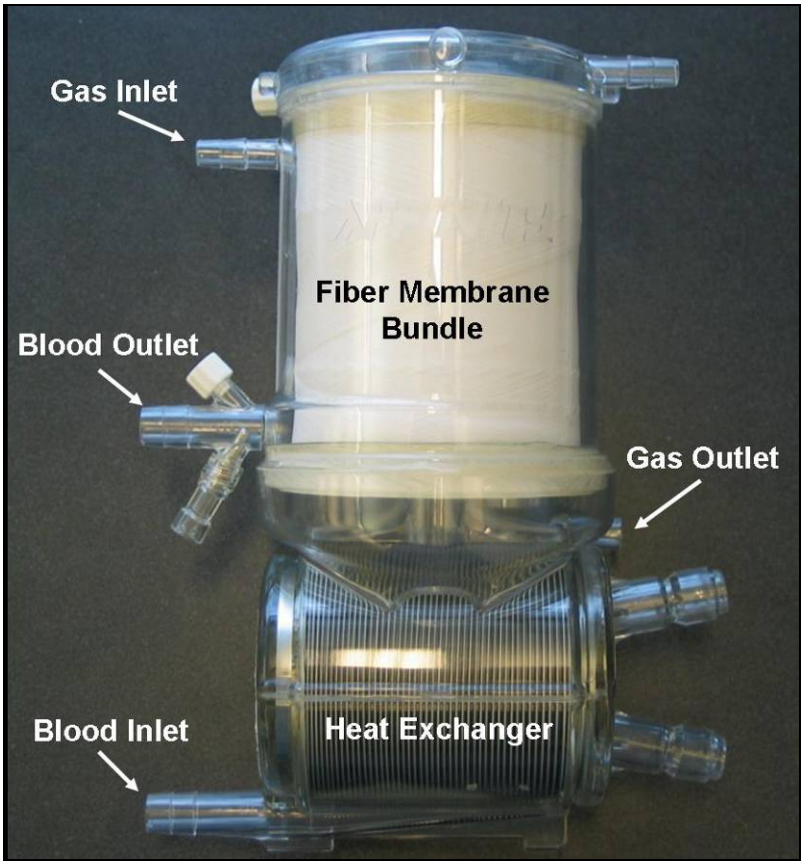

Figure 1-1: Membrane oxygenator.

ECLS is employed under circumstances of severe, reversible respiratory failure or to patients responding adversely to all advanced modes of mechanical ventilation. Operation of the circuit relies on a pump to draw blood from the vena cava, transport it through the membrane oxygenator, and return the blood either to the right atrium (venovenous bypass) or aorta (venoarterial bypass). Patients still receive mechanical ventilation while on ECLS, however settings are reduced to minimize VILI due to the ability of the oxygenator to exchange blood gases[13]. With less required work from the lungs, ECLS permits physiological complications to abate and the therapy can be applied for weeks barring complications. Further research for ECLS

is focused on creating pumpless systems that generate blood flow through the oxygenator by means of pressure gradient from the patient femoral artery to femoral vein ($AVCO_2R$)[14].

Limitations of ECLS primarily arise from external circuitry and artificial blood contacting surfaces. In order to avert thrombosis within the circuit, patient blood is continuously anticoagulated and bleeding is a major risk whether internal (intercranial) or from cannula dislodgement[13, 15]. Patients are paralyzed and/or heavily sedated to minimize movement causing dislodgement, which creates a high risk scenario for decubitis ulcers[15]. Also, the continuous exposure of the blood to artificial surfaces causes platelets to adhere and/or alter function (thrombocytopenia) requiring the patient to receive multiple platelet transfusions. In addition, the ECLS circuit must be constantly monitored for mechanical failures such as tubing degradation, oxygenator or pump failure, and presence of gaseous emboli or clot formation[16]. Other noted complications include sepsis and renal failure[15]. Finally, ECLS requires a multidisciplinary team to provide care. Staffing and overall cost of the procedure, as well as restriction to major medical centers are further limitations to providing this therapy.

Over the years, these therapies have been utilized to improve patient survival rates. A high mortality rate, however, still remains associated with ARDS and acute exacerbations of COPD. Further research and development for potential treatments is thus warranted.

1.3 PRINCIPLES OF HOLLOW FIBER MEMBRANE GAS EXCHANGE

Membrane oxygenators employ hollow fiber membrane (HFM) technology to achieve gas transfer. The HFMs are made from polymers such as polymethylpentane or polypropylene that

are extruded into microporous tubes. The miniature tubes are further arranged into bundles that comprise present-day oxygenators. Figure 1-2 displays a magnified view of the HFMs. Wall porosity enables the membranes to exchange oxygen and carbon dioxide gases while blood flows external to the fibers. The walls of the fibers are hydrophobic and prevent fluid from leaking into the lumens.

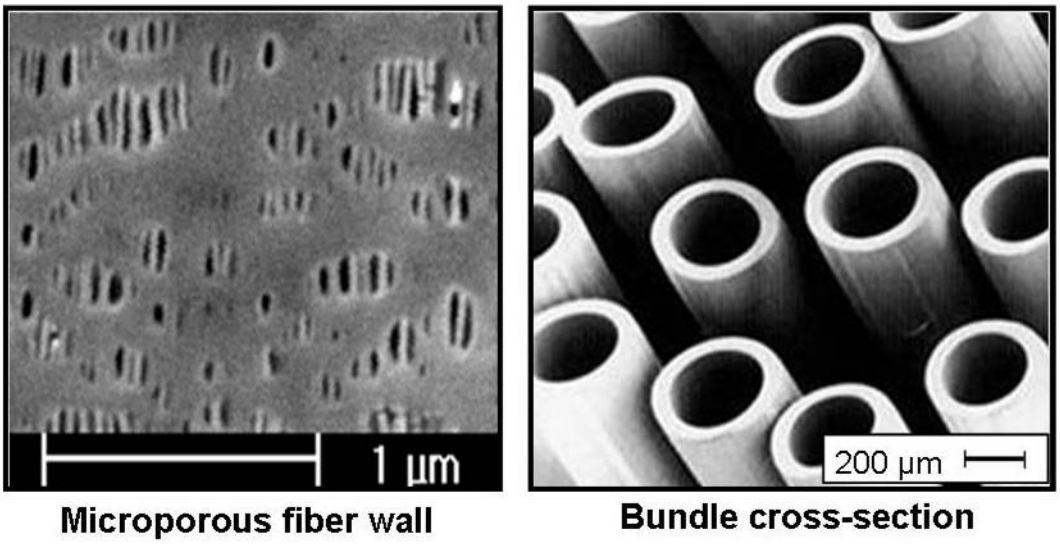

Figure 1-2: Porous wall structure of HFM (left), Bundle of HFMs (right).

The process driving gas exchange in the technology is diffusion. Oxygenators are setup to process venous blood that is high in CO_2 concentration and low in O_2 concentration. Pure O_2 gas is passed through the HFM lumens at a $pO_2 \approx 740$ mmHg. A transmembrane concentration gradient is thus created between venous blood (pO_2= 38 mmHg, $pCO_2 > 50$ mmHg)[17] and fiber lumen. The high concentration of CO_2 in the blood favors diffusion into the low concentration side in the HFM lumen, and conversely the high concentration of O_2 in the HFM favors diffusion into the low concentration blood-side. A schematic representing CO_2 diffusion is shown in

Figure 1-3. Blood passing through the HFM bundle is thus supplemented with oxygen and removed of carbon dioxide in a similar fashion to the natural lung.

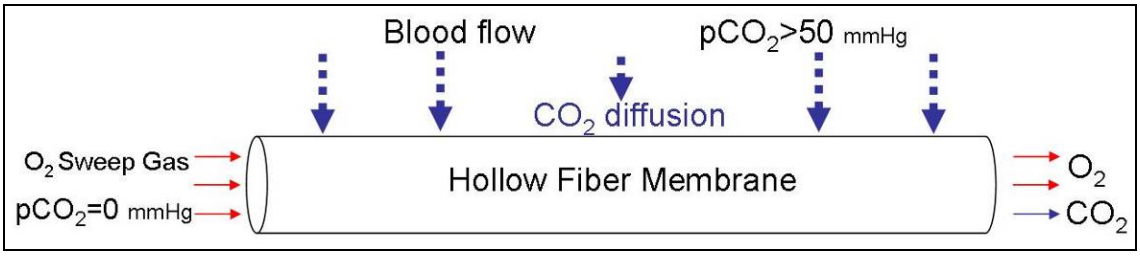

Figure 1-3: Blood-side CO_2 diffusion into the lumen of a hollow fiber membrane.

Factors regulating gas exchange in the oxygenator include gas partial pressures in both blood and fiber lumens, total HFM surface area, fiber bundle geometry and relative blood to fiber velocity. The main resistance to diffusion that limits gas exchange is the concentration boundary layer that forms near the external walls of the individual fibers. The layer forms as a result of blood flow patterns around the fiber walls. To increase oxygenator gas exchange then, additional surface area can be provided to boost overall diffusion or boundary layers can be reduced to decrease mass transfer resistance. High relative blood velocity to fibers facilitates boundary layer reduction.

Oxygenator devices can be categorized as either passive or active by the means in which boundary layer reduction is approached. Passive devices rely on blood flowrates and fiber bundle geometry to mix flow patterns and disrupt layer formation near stationary fibers. Active devices implement motion to the fiber membranes to obstruct boundary layer formation.

1.4 INTRAVASCULAR RESPIRATORY SUPPORT THERAPY

Intravascular respiratory support therapy refers to treatment employing an artificial lung within the vasculature of a patient to supplement lung function. The concept is an alternative approach to treating ARDS and was initiated by J.D. Mortensen[18-20]. A device, using the same HFMs as oxygenators, was envisioned to be inserted into the vena cava to process venous blood supply rather than situate extracorporeal as in ECLS. Figure 1-4 exemplifies the vessel placement. Access to the vena cava is gained through a peripheral vessel such as the femoral vein depicted in the figure.

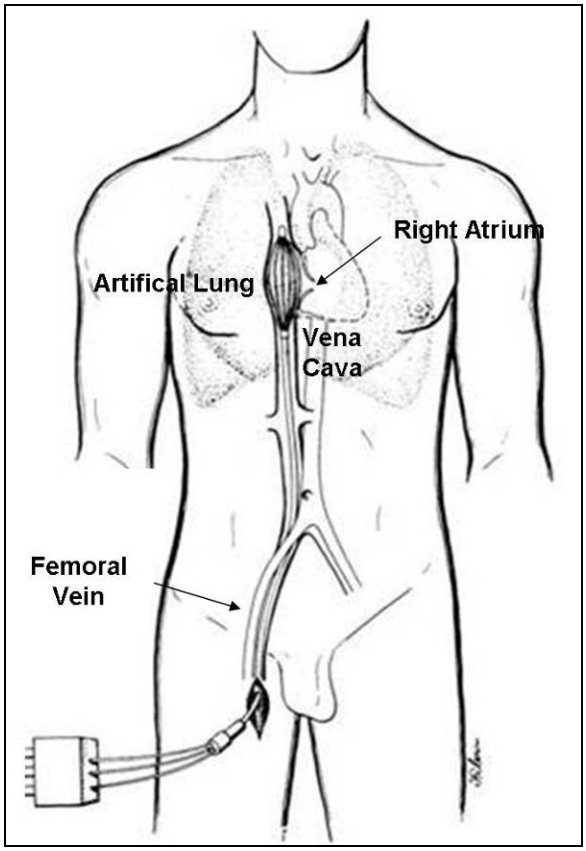

Figure 1-4: Schematic of intravascular artificial lung implant.

The workload of the diseased lungs to meet basal requirements is greatly reduced by artificially supplementing oxygen and carbon dioxide exchange prior to the lungs. This may allow a decrease in mechanical ventilation intensity to support patients, which has been shown to improve mortality rates[21]. Permissive hypoventilation is a protective strategy to prevent VILI and improve recovery but results in hypercapnia. Intravascular respiratory support limits hypercapnia by removing excessive CO_2 from venous blood and improving patient tolerance of hypoventilation[22]. Hattler and Federspiel state, "that a further reduction in ventilation, in a setting where all patients would tolerate the therapy and acute changes in pCO_2 levels would not occur, should lead to a consistent and even greater reduction in ventilator requirements and in mortality for patients in acute respiratory failure[23]."

The ability of intravascular respiratory support to facilitate carbon dioxide removal from the circulation provides an essential advantage over sole mechanical ventilation strategies. By regulating hypercapnia, intravascular respiratory therapy can eliminate the deleterious effects that often develop with mechanical ventilation. In addition, the diseased lung tissue experiences a lower workload since the device itself is performing partial respiratory function. The reduced workload allows the injured tissue to rest and may improve tissue recovery.

ECLS is able to regulate hypercapnia but is associated by the host of complications resulting form blood circulating outside the body. Utilizing an intravascular device eliminates external circuitry lessening the risks of thrombocytopenia and activation of complement due to artificial surfaces[24]. Less artificial surface can also result in lower anticoagulation levels thus decreasing bleeding risks. Overall implementation of the therapy would be easier than ECLS making it less demanding on hospital resources, less expensive, and available in more hospitals[23].

The device introduced by Mortensen for intravascular respiratory therapy was the intravascular oxygenator (IVOX). The IVOX consisted of a bundle of microporous HFMs coated with ultra-thin siloxane and covalently bonded thromboresistant bioactive molecules. The coating permitted selective permeability of carbon dioxide and oxygen gas while excluding blood constituents[19, 20]. Oxygen gas was shuttled into the HFMs under vacuum through a gas inlet limb of a double lumen transport tube. Exhaust gas from the device was returned through the opposite lumen. The HFMs of the IVOX were furled into a compact bundle for insertional purposes, and once placed in the vena cava were unfurled so that venous blood could flow through the exposed bundle[20]. Each individual HFM was crimped in order to create non-laminar flow through the device to decrease diffusional boundary layers[19]. This defined the IVOX as a passive device since only physiological blood flow patterns provided boundary layer disruption.

The IVOX remains the only respiratory catheter to undergo clinical trials, which occurred in the early 1990's. A total of 160 patients received IVOX devices with HFM surface areas ranging from 0.2-0.5 m^2. The average CO_2 and O_2 transfer rates were observed between 40-70 ml/min[25] corresponding to approximately 20-30% of adult resting basal requirement (250 ml O_2/min, 200 ml CO_2/min). Results from the trial indicated that respiratory support was marginal and gas exchange rates needed to be improved to an estimated 50% of basal requirement for beneficial clinical application[25, 26]. Development of the IVOX device later ceased.

Efforts to develop a respiratory assist catheter at the University of Pittsburgh began with the Hattler Catheter (formally referred to as the intravenous membrane oxygenator (IMO)). The key feature of the Hattler Catheter (HC) was a pulsating balloon situated within a bundle of HFMs. The catheter is depicted in Figure 1-5. A triple lumen conduit was used to transport

sweep gas through the fiber bundle and shuttle helium gas into the central polyurethane balloon. The unique active mixing imparted a convective radial flow through the bundle by pumping blood during corresponding pulsations, which consequently reduced fluid-side diffusional boundary layers[27, 28]. Pulsation was observed to significantly increase gas exchange rates by 200-300% at lower blood flow rates and 50-100% at higher flow rates in ex vivo testing of the device designed to compare against similar IVOX performances[29, 30]. More modest increases of 15-35% were observed in animal studies with a maximum CO_2 efficiency (gas exchange per unit area of HFM) of 282 ml CO_2/min/m^2 (HC surface area of 0.17 m^2) in sheep[31].

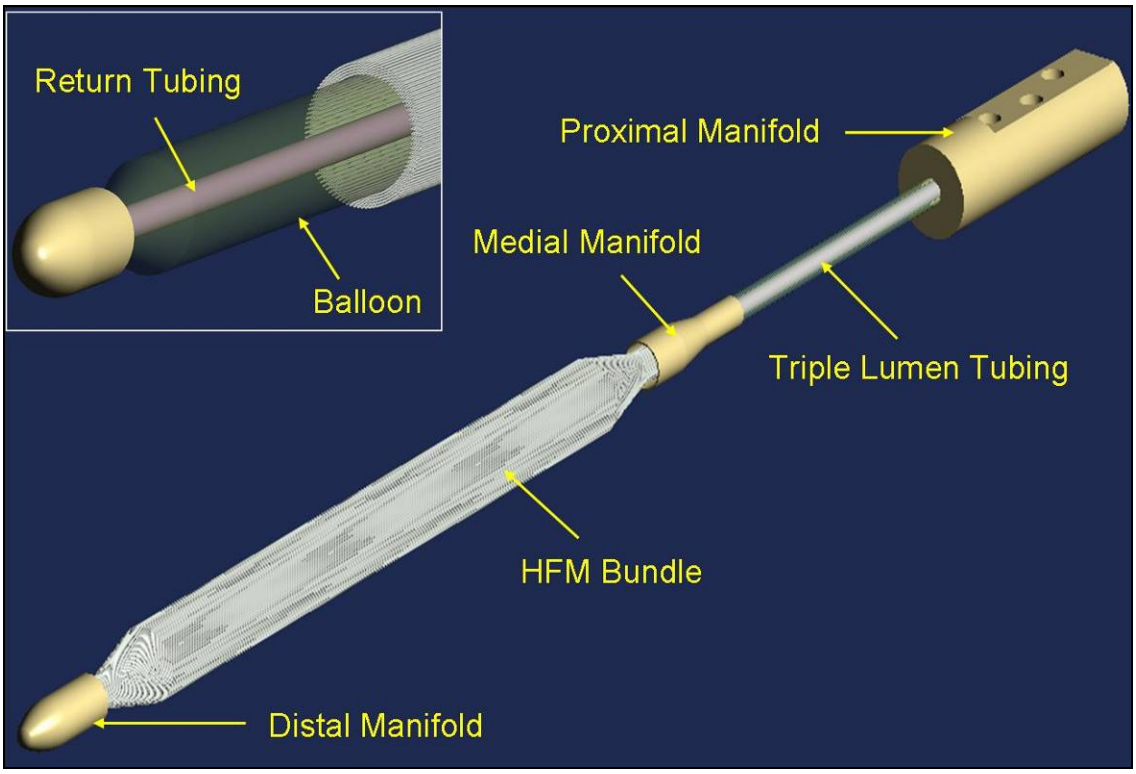

Figure 1-5: Hattler Catheter.

Investigations to further increase gas transfer efficiency looked into randomly pulsating the balloon but the effects were unsubstantial when compared to conventional, constant pulsation[32]. The catheter was 33 Fr in size and intended for percutaneous insertion but was still large in comparison to other medical catheters and likely required a specialized vascular surgeon for insertion. An ongoing project at the University is focused on making the system more widely available by reducing the catheter size so that critical care doctors or reasonably trained personnel can insert as well.

Researchers at Pennsylvania State University approached intravascular therapy by pursuing the Penn State Intravascular Lung (PENSIL) during the mid to late 1990's. The placement of the device was proposed to span the vena cava and extend through the right-side heart into the pulmonary artery. The improvement in gas exchange rates over IVOX would be achieved by processing more cardiac output due to pulmonary artery placement, increasing total surface area for exchange, and positioning HFMs for perpendicular blood cross-flow[33]. The PENSIL consisted of a central catheter through which oxygen gas was cycled by an oscillating pressure between 130-775 mmHg. Blind-ended HFMs were attached to the central catheter and required sweep gas to diffuse in and out of each fiber. The oscillating pressure was required to overcome diffusional resistances existing in the HFMs due to the absence of flow[34, 35]. Gas exchange efficiencies of 140 ml O_2/min/m^2 and 25 ml CO_2/min/m^2 (corrected to physiological pCO_2 driving gradient) were achieved in the PENSIL[28]. It was concluded that an additional mechanism for reducing blood-side boundary layers would be necessary in order for the PENSIL to further augment gas exchange and provide any clinical significance[34].

The intravascular lung assist device (ILAD) and dynamic intravascular lung assist device (D-ILAD) were two devices developed at Northwestern University. Research on the ILAD took

place in late 1980's. The ILAD concept consisted of HFMs arranged in cross-flow fiber units serially aligned along two silicone rubber gas conduits. The units could be radially expanded into a rosette-like configuration to minimize shunt flow around the device. Gas exchange results were promising with devices of 0.4-0.6 m^2 surface area transferring 100 ml/min of both O_2 and CO_2. Device blood flow resistance, however, was excessive and steps were undertaken to overcome the blood-side pressure drop[36].

The approach to improving the ILAD incorporated rotational and oscillatory movements of the device. The D-ILAD was fabricated from a sheet of HFMs attached to a central supporting shaft serving as the inlet and exhaust gas pathway. The shaft was twisted to configure the fibers into a helical screw-like arrangement along the length of the catheter[37]. The catheter was connected to a motor to rotate the entire device and pump fluid past. The combination of new fiber arrangement and rotation substantially reduced the fluid size pressure drop to < 5 mmHg[37]. Testing in bovine blood at roughly 2 LPM flowrates showed D-ILAD transfer efficiencies to be 208 ml O_2/min/m^2 and 310 ml CO_2/min/m^2 [38]. Plans were proposed to develop a stationary sheath for vena cava wall protection against device rotation, but efforts ultimately shifted to developing a total artificial lung device.

The highly integrated intravascular membrane oxygenator (HIMOX) is currently being investigated at the Helmholtz Institute for Biomedical Engineering in Germany. The device was introduced in 2004 and utilizes a micro-pump to drive blood through HFM modules[39]. The HIMOX incorporates similar ideas from the ILAD and D-ILAD and is comprised of serially arranged HFM units along a central catheter. Longitudinal compression of the device following insertion causes the fiber units to assume a highly-dense disc shape through which blood cross-flow can be achieved. The individual bundles are enveloped within an outer sheath that

maintains blood flow generated from the proximally located micro-pump situated in the inferior vena cava[40]. The pump is necessary to compensate for the blood flow resistance of the individual fiber units which exhibit pressure drops of 6-12 mmHg (porosity dependent) at porcine blood flow rates of 4 LPM. Oxygenation testing of individual bundles with surface areas of 0.013 m^2 have achieved efficiencies of 450 ml O_2/min/m^2 [41]. Future studies testing full devices of 10-15 bundle units in an animal model are proposed.

1.5 PERCUTANEOUS RESPIRATORY ASSIST CATHETER

The purpose of the percutaneous respiratory assist catheter (PRAC) project at the University of Pittsburgh is to develop a catheter with widespread clinical acceptance. To fulfill this end, the catheter must be safe, effective, and amenable to easy insertion. These criteria require the artificial lung device to be smaller than the 33 Fr (11 mm OD) size of the previously developed Hattler Catheter. An insertion size of 25 Fr (8 mm OD) or less is targeted for the PRAC device. The catheter is proposed for respiratory support of patients with acute or acute on chronic lung failure and is intended for short-term use of 1-2 weeks. The primary performance goal is CO_2 removal since sufficient oxygenation levels can be attained in the clinical setting through nasal oxygen or specific ventilation modes. Targeted CO_2 removal rates for the catheter are 75-85 ml/min under normocapnia conditions, which corresponds to about one-third of the normal basal requirements. The device will facilitate ventilatory lung protective strategies by regulating hypercapnia conditions. Removal rates are expected to increase near one-half of the basal requirement under permissive hypercapnia.

During insertion the catheter will extend through the femoral vein into the vena cava until it spans the right atrium of the heart. The location allows the device to process all venous blood returning from the major vessels of the body. Furthermore, flow from the vena cava into the right atrium creates an additional blood mixing component since cross-flow will occur. This mixing regime may influence boundary layer formation.

Pure oxygen gas will be shuttled through the HFM bundle under a vacuum so that O_2 transport occurs by diffusion only. The vacuum ensures that oxygen sweep gas is not bubbled through the pores into the blood because of a high transmembrane pressure gradient. Manifolds at the proximal and distal ends of the fiber bundle will collectively organize the fibers to permit sweep gas flow in parallel through the bundle. Conduits connecting to and from the manifolded bundle will create a single, continuous flow path for sweep gas. Flowrate through the device will be maintained in adherence to the analysis of Federspiel and Hattler which determined that gas flowrates through oxygenators must be 40-60 times greater than the CO_2 exchange rate in order to achieve maximum efficiency[42]. Lower flowrates lead to CO_2 accumulation within the HFMs which reduces the gas concentration driving gradient responsible for diffusion. The 40-60 guideline assures that gas transfer is maximal and not dependent upon sweep gas flowrate.

Finally, the device will be operable without causing harmful effects to the blood. Actively mixing the blood can cause hemolysis if erythrocytes experience excessive shear stresses and exposure times. The catheter will be designed to minimize hemolysis and maintain blood plasma free hemoglobin (PFHB) levels, an index of hemolysis, below 15 mg/dL which is generally considered to be an acceptable level.

In reducing the insertion size of the catheter, there is a resultant loss in HFM surface area. The loss would be detrimental to performance if transfer efficiencies matched those of the

Hattler Catheter. In order to develop a smaller intravascular respiratory device, a different active mixing approach must be incorporated to further reduce concentration boundary layers-this would counterbalance the loss of HFM surface area so that overall gas exchange is not affected. The focus of this thesis was to evaluate rotational mechanisms to provide the enhancement in catheter efficiency. The potential for rotation to increase the relative velocity of fibers to blood over the pulsating balloon was great when considering servomotor technologies. An improvement in CO_2 efficiency generated from rotation would allow the desired reduction in catheter size.

Two rotational concepts were researched in this thesis. Each concept possessed differing characteristics and it was imperative to distinguish the effects of trade-offs between the two. The first employed a rotational HFM bundle. The concept design enabled a bundle to be fabricated to insertion size diameter and maximize HFM surface area. A drawback, however, was the necessity to protect the vessel from contact with the bundle. An effective safety mechanism to accompany the device during implantation, therefore, had to be developed. The second concept utilized a rotating impeller to distribute fluid through the bundle. The impeller was designed within the concept so that the bundle would remain stationary and enclose the rotating components. In comparison to the rotational bundle, the configuration eliminated the need for a safety structure, but the volume occupied by the impeller reduced overall HFM surface area.

Both concepts were researched to assess the benefits, shortcomings, and feasibility of using rotational actuation to develop a percutaneous respiratory assist device. Varying methods in assessing the two prototypes were conducted due to the differing concept characteristics.

Goals of the thesis were to:

- Analyze CO_2 removal levels of prototypes *in vitro*
- Evaluate hemolysis levels associated with operation
- Determine effective designs for conducting *in vivo* calf implants
- Perform acute calf implants to assess overall concept performance

Chapter 2 of the thesis discusses testing and results of the rotational bundle concept. Prototypes used in bench-testing and implants are described followed by the methods and results of bundle rotation and safety structure evaluative tests. In Chapter 3 the impeller prototype is highlighted. Feasibility studies and results are described. Chapter 4 will draw overall conclusions between the two concepts and the Hattler Catheter.

2.0 ROTATING FIBER BUNDLE CATHETER

Augmenting gas exchange efficiency using a radically differently process to balloon pulsation was first attempted through fiber bundle rotation. The concept for the catheter was to actively mix blood by attaining bundle speeds in far excess of devices researched previously (e.g. DILAD; 500 RPM). The rotation was hypothesized to raise device efficiency by increasing both the relative velocity of fibers to blood and venous blood mixing due to the swirling effect of the rotating bundle. A protective mechanism to safeguard the vena cava from detrimental contact with the catheter was simultaneously researched as well.

A bench-test prototype and implantable prototype for *in vivo* studies were developed during the evaluation process. Tests such as CO_2 exchange versus rotation, hemolysis, acute *in vivo*, and tortuous loop operation were performed to assess the feasibility of the concept. The testing methods and results are outlined in the following chapter.

A conceptual drawing of the rotational catheter is depicted in Figure 2-1. The catheter consisted of three manifolds to separate gas pathways and house necessary rotational components. The proximal manifold was used to introduce oxygen sweep gas and provide a port for exhaust gas removal. It also served to couple the device driveline to a servomotor. The medial and distal manifolds housed bearings and seals to stabilize rotation and prevent fluid entry into the device. These manifolds were stationary during operation providing a base to

attach a protective cage structure to the catheter. Also to note was hollow tubing running through the center of the HFM bundle. The tubing supported the bundle, was attached to the driveline, and provided an exhaust gas conduit from distal to medial manifold. Flow through the device was driven by a vacuum pump connected to the proximal manifold exhaust port. A DC servomotor and amplifier provided the required torque to actuate and control the catheter.

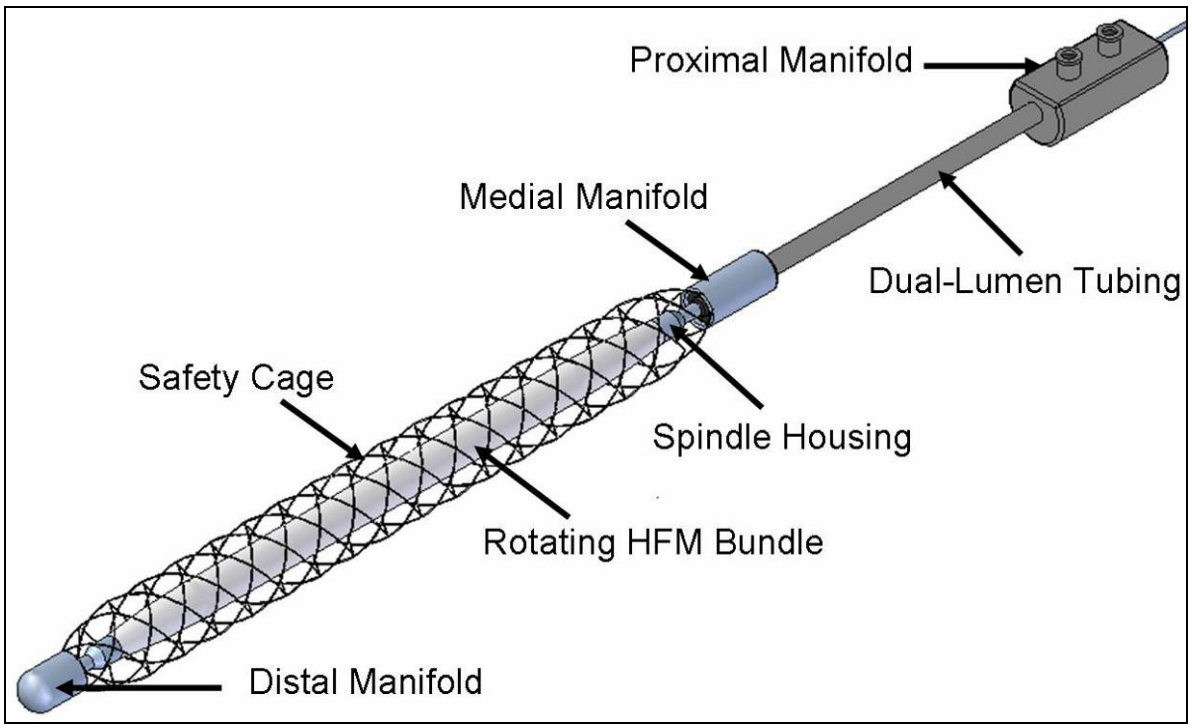

Figure 2-1: Rotational bundle catheter concept.

2.1 DESIGN AND FABRICATION

Three prototypes were used to evaluate the rotational bundle concept. Carbon dioxide removal characterizations and hemolysis tests were performed with the bench-test prototype to assess initial rotational bundle performance. Promising data from these studies led to the design of an implantable catheter for testing in an animal model. A final implantable prototype was fabricated to improve upon deficiencies observed with the previous version. Each of the prototypes are detailed with emphasis on components associated with the rotational design. The successive designs extended design considerations from the predecessor prototypes and therefore all three are similar. A brief summary of rotational bundle fabrication and materials used in prototype manufacture follows.

2.1.1 Prototype Designs

Bench-test prototype: RP

The first rotational PRAC (RP) prototype was fabricated to obtain bench data. The prototype was devoid of a safety cage and originally developed to easily interchange fiber bundles. For this reason, the prototype contained simple plastic manifolds and exhaust gas exited through distal tubing rather than being returned through the device. Celgard ARX30-240 HFM fabric was used to manufacture the bundle. Table 2-1 contains the fabric and bundle characteristics. The bundle was centrally supported by hollow stainless steel tubing running the length of the bundle. The tubing was coupled to a solid 0.037" diameter stainless steel drive shaft to transmit motor torque and rotate the bundle.

Table 2-1: HFMs (left) and rotational bundle (right) characteristics.

ARX30-240 HFM			**Rotational HFM Bundle**	
Material	Polypropylene		Bundle Length (cm)	20
Outer Diameter (μm)	300		Uncompressed Outer Diameter (mm)	10
Inner Diameter (μm)	240		# of Fibers	525
Average Pore Size (μm)	0.03		Fiber Layers	11
Porosity (%)	40		Wefts	Every other removed
Fibers per Inch (FPI)	54		Surface Area (m^2)	0.10

A sealed vacuum was used to drive oxygen flow from inlet to exhaust gas outlet. The sweep gas flowrate requirement for a prototype exchanging 75 ml CO_2/min was 3-4.5 LPM according to the 40-60 criteria previously mentioned[42]. The main resistance to flow in the RP was the HFM bundle and the resistance was estimated according to the following equation assuming oxygen as compressible gas[43]:

$$P_o^2 - P_L^2 = 2\left(\frac{128\mu L}{N\pi d^4}\right)P_{atm}Q^{RTP} \quad (1)$$

where P_o is upstream pressure, P_L is downstream pressure, μ is gas viscosity, L is fiber length, N is total number of fibers, d is fiber inner diameter, P_{atm} is atmospheric pressure, and Q^{RTP} is sweep gas flowrate (LPM). For a flowrate of 3.5 LPM, the corresponding pressure drop over the bundle was approximately 50 mmHg. The vacuum pump was capable of producing 9 LPM flow at this pressure head, and therefore the bundle design was adequate to attain sufficient sweep flow while leaving excess room for additional resistance in the implantable design.

Both medial and distal manifolds housed a seal and 2 bearings. Nitrile rubber rotary seals (#711801, Chicago Rawhide) for shaft ranges of 0.180-0.210” were press fit into the manifolds and can be viewed in Figure 2-2. These seals had a 0.375” outer diameter and 0.094” seal width. Lubricant (O-Lube, Parker) was applied to the rotational shafts to reduce friction with the seals. A smaller nitrile seal (#711800, Chicago Rawhide) for shaft ranges of 0.110-0.140” was placed in the proximal manifold to prevent atmospheric air leakage. Dual shielded ball bearings (0.1875” bore, 0.3175” OD) (#35380872, MSC Industrial Supply Co.) in the distal and medial manifolds stabilized bundle rotation. Similar smaller MSC bearings (0.1250” bore, 0.2500” OD) (# 35380815, MSC Industrial Supply Co.) were placed in the proximal manifold to maintain drive shaft concentricity.

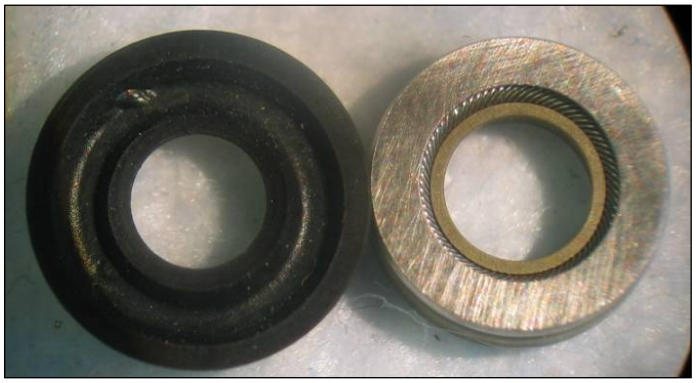

Figure 2-2: Chicago Rawhide nitrile seal (left), Bal teflon seal (right).

A high-speed electromechanical drive system was used for mechanical actuation. A brushless DC-servomotor (Series 2444-024B, MicroMo Electronics Inc.) and 2-quadrant PWM servo amplifer (Series BLD 3502, MicroMo Electronics Inc.) provided rotation and control. A conditional analog voltage of 0-5 volts set by a potentiometer dictated motor speed. The unit was

powered by a 24 volt AC/DC quad output power supply (Series NFS110-7602P, Artesyn Technologies). The components were housed within a single box for ease of use and protection from electrical failure. The unit contained a mini DC cooling fan to remove heat from the power supply. The controller box is displayed in Figure 2-3. Motor speed was measured with a digital rate indicator (Model CUB5, Red Lion Controls). A wire connection was introduced to the amplifier to tap voltage pulses returning from the servomotor hall-sensors. Connection from the amplifier to the digital rate indicator enabled pulses to be counted and displayed. A means for measuring motor torque was also included in the setup. The torque generated by the servomotor was directly proportional to the current requirement for motor operation. A wire connection was made to directly measure the DC current output from power supply to amplifier. The measurement was representative of the supplied current from amplifier to motor and was used to calculate motor torque by the servomotor torque constant. Finally, a fuse was placed in series from power supply to amplifier. The fuse automated the system to shutdown upon motor stall and protected the motor from damaging current levels.

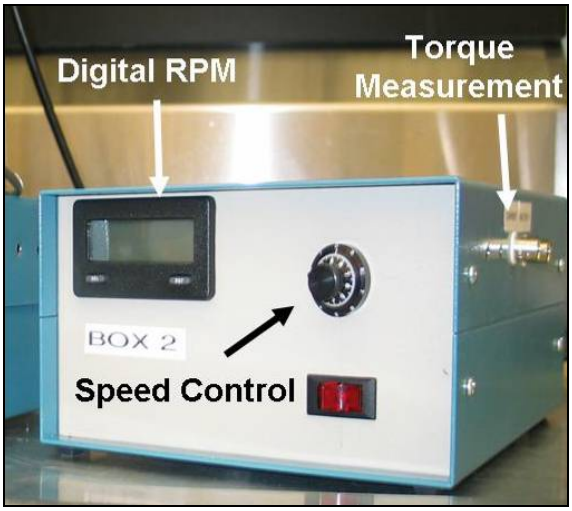

Figure 2-3: Servomotor controller.

Implantable prototype 1: RPI-1

Many of the components used in the RP device, including the HFM bundle, were directly transferred into the implantable prototype (RPI-1). The RPI-1 design was identical to the concept drawing in Figure 2-1. The major changes from RP were the addition of a safety cage structure and capped distal manifold to redirect sweep gas back through the central bundle conduit for removal at the proximal manifold. Medial and distal manifold material was changed from plastic to stainless steel for strength.

Super-elastic nitinol with a wire diameter of 0.019" was purchased (#NW-019-36, Small Part Inc.) to use for the safety cage. Nitinol material was selected because of its established biocompatibility and shape memory properties. Twelve wire stands were woven together to produce a 12" length stent and is viewed in Figure 2-4. The shape memory and elasticity allowed the stent to be compressed within an introducer sheath prior to insertion and expand back to shape once introduced within the vena cava. The diameter of the stent in an uncompressed state was 0.800", and the cage was fixed to the prototype at the medial and distal manifolds.

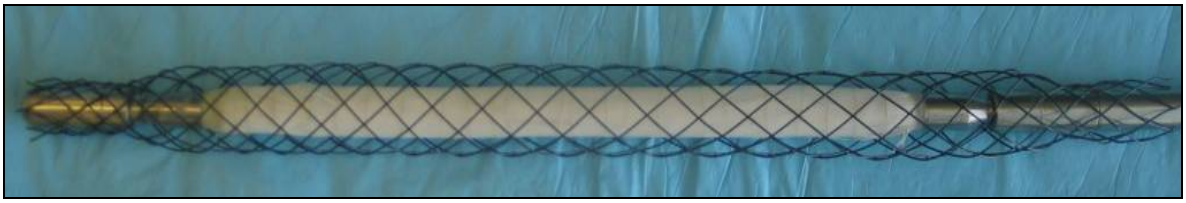

Figure 2-4: RPI-1 nitinol weave safety cage.

The nitrile rubber seals in RP were replaced with custom teflon rotary seals (#x225501, Bal Seal Engineering) shown in Figure 2-2. The seals produced less friction than nitrile seals because of seal material and did not require lubrication. They also contained a loaded spring that

applied pressure to the seal lip for maintaining interference with the bundle shaft. The seals were specified for 0.187" shaft diameter and 0.375" gland diameter.

Implantable prototype 2: RPI-2

The overall insertion size of the RPI-1 prototype during the animal study exceeded the 25 Fr design requirement due to the additional safety cage and introducer sheath thicknesses. The resultant design change was to lengthen the HFM bundle by 50%, or 10 cm. This reduced the overall bundle diameter and number of fibers to 350 but maintained a surface area of 0.1 m^2. The change proved to be a crucial factor in evaluating rotating bundle feasibility. RPI-2 was only ever tested on the bench. The device was reduced in diameter and lengthened, rather than just decreased in diameter, because gas exchange efficiencies confirmed that a loss of surface area would handicap overall CO_2 removal rates too much to overcome and reach targeted goals.

Testing of RPI-1 also revealed that the device was too rigid for both insertional and operating conditions. In order to perform within an animal model, increased flexibility was needed. The changes were implemented to both the central bundle tubing and solid drive shaft. The bundle tubing was replaced with reinforced plastic tubing that performed well in tortuous loop tests described in Appendix A for the then parallel impeller catheter development (Chapter 3.0). New England Wire Technologies tubing was used and properties of the tubing are detailed in Table 2-2.

Table 2-2: New England Wire Technologies tubing.

Part #	N98-TOL-664
Topcoat Material	Blue Pebax
Reinforcement Braid	44 AWG Type 304 Stainless Steel
Inner Diameter (inches)	0.057
Outer Diameter (inches)	0.081

The solid stainless steel drive shaft was replaced with a bi-directional coil shaft (B.W. Elliott Manufacturing Company). The coil design transmitted torque better and maintained an operable drive line under bending conditions.

Finally, limitations of the RPI-1 safety cage were addressed. Briefly, the stent was easily displaced in lateral and vertical directions, and only provided concentric hoop strength protection from the rotating bundle. An effort to stiffen the nitinol focused on applying heat treating procedures but proved unsuccessful in providing sufficient strength to oppose point forces. Redesign of the safety cage centered on bridging 316 stainless steel solid tubing (0.036" diameter) from the medial to distal manifold. Much of this effort was undertaken by a summer student assisting on the project. Thicker tubing and material change strengthened the cage by increasing the tubing aspect ratio (thickness/length). Four cables spanned the HFM bundle, and additional tubing was attached to the medial and distal manifold to center the device within a vessel.

2.1.2 Fabrication

Manufacture of protoypes was the primary responsibility of the lab fabricator, Mr. Brain Frankowski. A description of hollow fiber bundle production is presented. The materials necessary for fabricating prototypes are also addressed.

The fabrication of a HFM bundle began by determining the desired surface area. The number of fibers needed was also determined; the central bundle tubing outer diameter and total allowable device diameter were taken into account in order to estimate fiber number. This knowledge provided the fabricator information to calculate a desired fiber length.

A specified length of HFM fabric accounting for the necessary fiber count was then unrolled from the supply. A razor was used to cut the wefts of the fabric to separate the mat from the supply, and following, several individual HFM were removed from each end of the mat to ensure that no fibers were damaged during the cutting process. Note the wefts were threading that maintained the individual HFMs in a fabric sheet. A perpendicular cut to the mat leaving an extra 5 cm extra to the desired fiber length was then made.

The bundle mat was removed of wefts. The weft ends were untied with tweezers and pulled from the mat to remove every other one. Devcon 5 minute epoxy was applied to the central tubing and the tubing was placed along the length of the prepared mat edge. The tubing and mat were rolled into a bundle so that wefts aligned. A 2:3 w/w epoxy mixture of vorite and polycin respectively, was applied to the loose wefts adjacent to the last fiber in the roll in order to constrain the roll. The loose fiber ends were then bound with cotton thread to form two 1 cm cuffs.

Delrin molds were fabricated to manifold the fiber bundle ends. The cuffs of the fiber bundle were placed in the molds and the aforementioned epoxy mixture was injected. Upon curing the delrin molds were removed and a cut through the mold was made to expose the internal tubing. The resulting bundle contained two ends with patent fibers that were externally glued together along the length of the thread cuff.

The following materials were used in part fabrication and device assembly. The majority of prototype components were manufactured from 316 stainless steel. These parts included drive related components and those making up the distal and medial manifolds. The parts were formed by the fabricator on a Hardinge lathe. Tubings used as gas pathways between proximal and medial manifolds were made of polyurethane plastic. The proximal manifold was shaped from acrylic. As mentioned previously, both 316 stainless steel and nitinol were trialed as safety cage materials.

The majority of assembly required the use of the polycine and vorite epoxy mixture (2:3 w/w respectively). This included fiber bundle fixation to stainless steel components and tubing mating at the medial and proximal manifolds. Stainless steel components were also connected together with the epoxy. Permeatex clear RTV silicone adhesive sealant was utilized along the outer diameter of the seals to anchor in place and provide additional sealant. Drive shaft components were attached using silver solder.

2.2 EVALUATIVE TESTS

The catheter prototypes were subjected to a series of tests to assess using a rotational bundle as an avenue to actively mix the blood. Testing was first conducted on the bench to observe the overall CO_2 removal ability of the concept. Results showed promise and a second study was pursued to examine concept biocompatibility since rotating a bundle at high-speed rates had the potential to damage red blood cells because of high shear stress exposure. Insight into blood biocompatibility was imperative before further advancing the concept. The development process

proceeded from the bench to realize catheter operation in an animal model. *In vivo* evaluation revealed prototype design deficiencies and research was brought back to the bench to address the shortcomings. The implantable prototype was tested in a tortuous configuration similar to that observed in the implant. The following section describes the testing methods applied in evaluating the rotational bundle concept.

2.2.1 Gas Exchange

The gas exchanging ability of the catheter was evaluated on the bench using the RP prototype. The *in vitro* test was an idealized simulation of the vena cava environment and provided rapid device characterizations allowing device to device comparisons and indication of trends that could be observed *in vivo*. RP characterizations were performed to analyze CO_2 transfer versus RPM rate, and to test a design fix to eliminate micro-bubble formation. Micro-bubbles formed near the rotating HFMs because local water pressure was reduced to below the sweep gas pressure at high speeds causing oxygen gas to bubble, rather than diffuse, into the fluid medium. This phenomenon is observed in Figure 2-5.

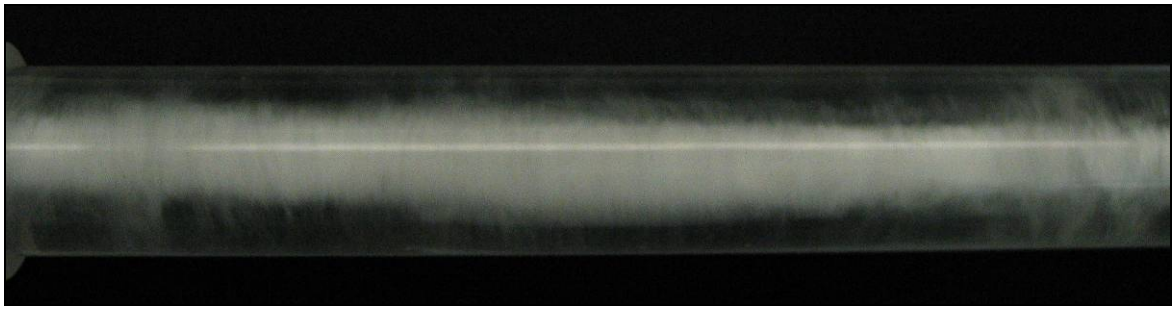

Figure 2-5: Micro-bubbles expelled from a rotating HFM bundle.

Testing was performed by introducing the device into separate fluid and gas circuits. The fluid loop re-circulated de-ionized water past the device. Water was thus the blood representative fluid and served as the gas carrying medium. Briefly, the RP prototype was placed in the fluid circuit within a 7/8" diameter acrylic test section that crudely simulated the vena cava. The fluid circuit contained a reservoir, fluid pump, thermometer, heater, flow meter, pressure transducer and de-oxygenator, and all were connected with standard laboratory tygon tubing. A schematic of the setup is shown in Figure 2-6.

The de-oxygenator was used to establish test section water inlet conditions. Conditions set were a pO_2 of 25-35 mmHg and a pCO_2 of 47-53 mmHg which represented physiological normocapnia venous blood. The water conditions were monitored on an ABL 555 soluble gas analyzer machine. Water flowrate through the loop was maintained at 3 LPM with a temperature of 37 ˚C, and the water gauge pressure within the test section was kept near 100 mmHg to prevent oxygen micro-bubble formation.

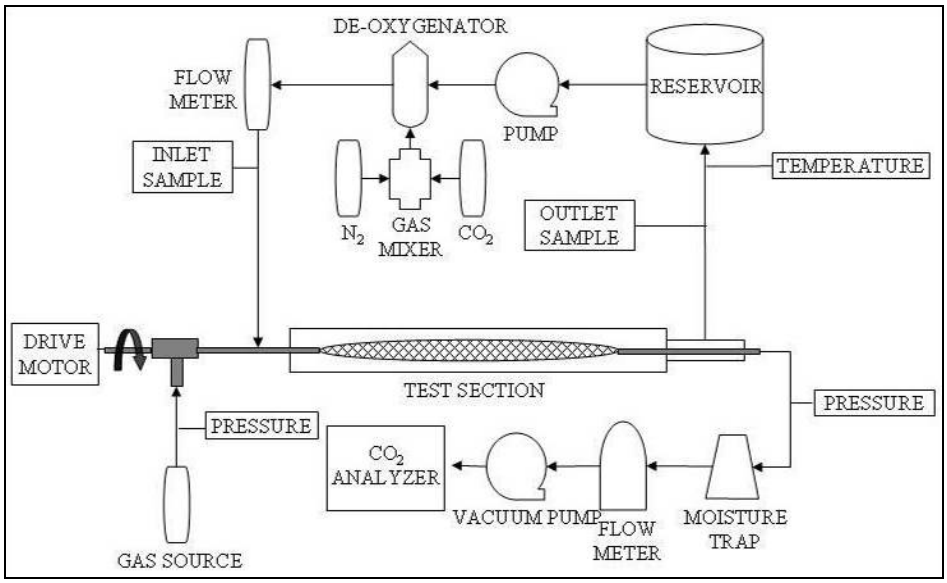

Figure 2-6: *In vitro* gas exchange schematic [44].

The gas circuit established the pathway for oxygen sweep gas introduction and exhaust gas analysis. The device inlet was connected to a pure oxygen source maintained at atmospheric pressure. Upon exiting the device the sweep gas was passed through a cold moisture trap for dehumidification, and following it was directed through a flow meter and CO_2 analyzer. The flowrate was driven by a vacuum pressure station that pulled sweep gas through the entire circuit. Gas pressure drop over device inlet to outlet was monitored using a pressure transducer. Table 2-5 contains all equipment used in gas exchange testing.

Table 2-3: *In vitro* gas exchange test equipment.

Component	Model	Manufacturer
CO_2 analyzer	CO_2-44	Physio-Dyne Instrument Corp.
Magnet fluid pump	MD-30RZT-115N201	Iwaki Walchem Corp.
Gas vacuum pump	400-3910 air cadet station	Barnant Co.
De-oxygenator	Adult hollow fiber oxygenator	Shiley Inc.
Gas flow meter	Top Trak 821-1	Sierra Instruments Inc.
Thermometer	Digi-sense type T thermocouple	Cole-Parmer Instrument Co.
Water pressure transducer	X771-025DT	Omega Engineering Inc.
Gas pressure transducer	143SC	Honeywell International Inc.
Gas analyzer	ABL 555	Radiometer Copenhagen

The method for gathering gas exchange data is summarized as follows. Water conditions were first measured to ensure that inlet pCO_2 and pO_2 were within desired range. Acceptance of inlet conditions was followed by recording of water temperature, flowrate, and pressure in the fluid circuit. Also, the sweep gas flowrate, device pressure drop, motor torque, and exhaust CO_2 concentration were recorded. The RPM rate was then changed and the procedure was repeated to obtain a minimum of two random data points for each RPM to ensure repeatability.

CO_2 removal, V_{CO2}, was calculated for the rates by the following equation:

$$V_{CO2} = Q^{STP} F_{CO2} \qquad (2)$$

where Q^{STP} is the flowrate of sweep gas at standard temperature and pressure and F_{CO2} is the fraction of CO_2 in the exhaust of the catheter, as measured per the CO_2 analyzer. The exchange rate was then divided by the HFM surface area and normalized to the target pCO_2 inlet of 50 mmHg to calculate efficiency (VCO_2) and normalize variability associated with small changes in inlet pCO_2 concentrations:

$$VCO_2 = V_{CO2} \frac{50}{pCO_2^{INLET} \bullet SA} \qquad (3)$$

The design addition eliminating micro-bubble formation in the RP was also examined by measuring gas exchange. The procedure however, was performed at both water pressures of 100 mmHg, and 10 mmHg to allow bubble formation. Additionally, a resistance was added to the sweep gas inlet. Briefly, standard control gas exchange was first measured at various RPM rates at 100 mmHg water pressure to eliminate micro-bubble formation. Following, the pressure was decreased to 10 mmHg to measure gas exchange influenced by micro-bubble formation. Finally, the sweep gas resistance at the device inlet was increased without altering the flowrate, and CO_2 exchange was again measured at 10 mmHg water pressure. The three sets of data were compared to evaluate the design fix.

2.2.2 Hemolysis

A major biocompatibility concern for the rotational bundle concept was the effect rotation would have on erythrocytes in the blood. Two hemolysis tests were performed to assess whether the

concept of rotating a HFM bundle would be feasible with biocompatibility. It is important to highlight that the tests were not undertaken to assess total prototype biocompatibility (i.e. seals and safety cage) since the catheter was still in early developmental stages. The two studies evaluated hemolysis generation by comparing to a Datascope Intra Aortic Balloon Pump control device. The Datascope IABP is a clinically used vascular device with known hemolysis levels making it an appropriate control.

Bovine blood was obtained from a slaughterhouse the morning of testing. The blood was filtered using a 40 μm microaggregate blood transfusion filter immediately following collection. Gentamicin (0.1 g/ml) and Penicillin (500,000 U/ml) were added to the filtered blood to prevent bacterial growth. The blood was also anticoagulated with anticoagulant citrate dextrose in a 9:1 ratio respectively to prevent clotting during testing.

A test loop for each device was setup with 7/8" diameter test sections. All components were connected using standard laboratory tygon tubing. A schematic of the loop is shown in Figure 2-7. Blood was pumped from a reservoir and heated to 37 ˚C before entering the test section. Each test loop was run for six hours with the collected bovine blood. A blood volume of 1.5 L was used in each loop and re-circulated at 3 LPM. The IABP was pulsed at 180 BPM and the RP protoypes were rotated at 7,500 RPM. No sweep gas was run through the prototypes although a slight vacuum was applied to evacuate any residual air in the HFMs. Table 2-4 contains pertinent information regarding equipment used.

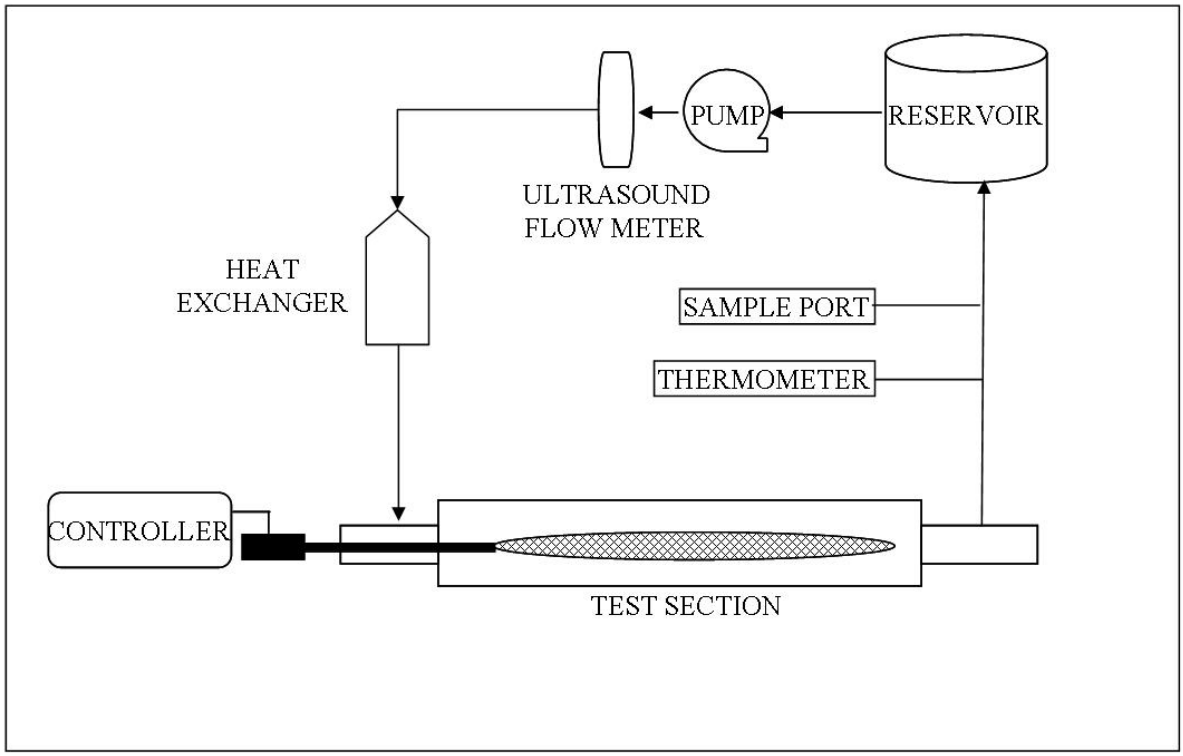

Figure 2-7: Hemolysis circuit schematic.

Table 2-4: Hemolysis test equipment.

Component	Model	Manufacturer
Blood transfusion filter	SQ40S	Pall Biomedical Inc.
Ultrasonic flow probe	T110	Transonic Systems Inc.
Reservoir bag	Affinity reservoir bag #321	Medtronic Inc.
Blood pump	Biomedicus biopump BPX-80	Medtronic Inc.
Pump console	540 Bio-console	Medtronic Inc.
Pediatric heat exchanger	D1078	Medtronic Biotronics
Gas vacuum pump	400-3910 air cadet station	Barnant Co.
Dry chemistry system	Spotchem EZ SP-4430	Arkray Inc.
3,800 RPM centrifuge	Centrific model 228	Fischer Scientific Int. Inc.
10,000 RPM centrifuge	Galaxy 7	VWR International
Spectrophotometer	Genesys 5	Thermo Spectronic
Thermometer	Digi-sense type T thermocouple	Cole-Parmer Instrument Co.
Temperature Pump	T/Pump TP-406	Gaymar Industries

Fragility indices were calculated according to Lund et al. to characterize blood batches prior to testing[45]. Blood protein levels were measured in a dry chemistry system since it was shown that blood proteins have a protective effect for RBCs[46]. Outlet blood samples were taken from each loop every half-hour for the first 2 hours and then every hour for the remaining 4 hours. Hemotacrit and plasma free hemoglobin measurements were made for each sample.

To obtain PFHB, whole blood samples from the loop were centrifuged at 3,800 RPM for 15 minutes. The plasma was siphoned from the sample, and centrifuged again at 10,000 RPM for 15 minutes. This plasma was then re-spun again for 15 minutes at 10,000 RPM. Following, the sample was placed in a spectrophotometer for measurement.

A de-ionized water sample was used as a reference and PFHB absorbance was measured at a wavelength of 540 nm. PFHB levels were calculated by converting the absorbance readings according to the equation:

$$\text{PFHB (mg/dL)} = [125\ (\text{mg/dL}) * \text{Abs}] - 5\ \text{mg/dL} \quad (4)$$

where 125 mg/dL is the conversion factor for bovine blood and 5 mg/dL is a background reading when using DI water as a reference[45, 47]. This empirical relationship was determined previously by making serial dilutions of hemolyzed bovine blood.

2.2.3 Safety Cage and Implantable Prototype

Bench gas exchange and hemolysis results warranted development of an implantable prototype, RPI-1. The prototype was evaluated in a calf but deficiencies in application were exposed and

the study was unsuccessful in gaining gas exchange and hemolysis data in a physiological setting; therefore methods are not described. The test, however, was important in determining specific improvements the prototype needed in order to successfully manage an *in vivo* setting.

The RPI-2 prototype was tested in a tortuous bench loop setup to evaluate rotational operation and safety cage protection. An acrylic test section was fabricated to represent conditions observed in the *in vivo* bovine study. The section was made with two severe bends with increased bending radii to add a factor of safety in testing operation. A catheter capable of performing in the configuration would manage the more accommodating vasculature *in vivo*. Figure 2-8 represents the test section. RPI-2 was inserted into the section to span the curvature and performance was observed. Actual photos of the test section are viewed in Appendix A.

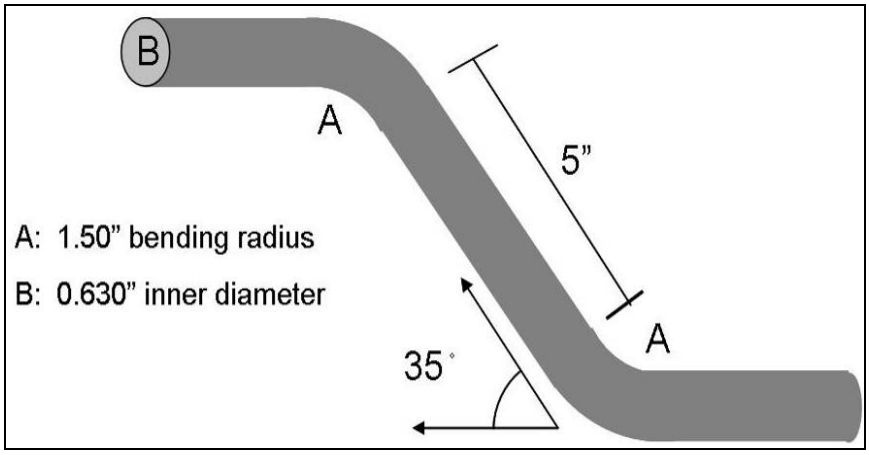

Figure 2-8: Dimensions of the tortuous test section.

2.3 RESULTS AND DISCUSSION

2.3.1 Gas Exchange

The *in vitro* gas exchange characterizations showed the rotational bundle efficiency to be greatly enhanced over the Hattler Catheter. Maximum efficiency for the RP prototype was 450 ml CO_2/min/m^2 [44] in comparison to 230 ml CO_2/min/m^2 of the balloon catheter (SA: 0.17 m^2, 40 cc balloon). This corresponded to a 2-fold increase in gas exchange efficiency. The doubling of efficiency was attributed to the differences in active mixing between the two devices. The rotational bundle achieved maximum gas removal near 7,000 RPM while the balloon catheter peaked at 300 BPM. The corresponding frequencies were 117 Hz and 5 Hz, RP and Hattler Catheter respectively, and the higher frequency indicated increased relative velocity of fiber to fluid which decreased mass transfer boundary layers. The active mechanisms were different between the two in that the RP catheter achieved bundle fluid penetration through rotational means whereas the balloon catheter positively displaced fluid through the bundle. Therefore the differences in frequency were not proportional to the changes in efficiency. A plot comparing RP VCO_2 versus RPM to maximal Hattler Catheter VCO_2 is viewed in Figure 2-9. VCO_2 was a function of RPM rate for the rotational but efficiency plateaued near 7,000 RPM and was markedly similar as RPM exceeded the critical rate.

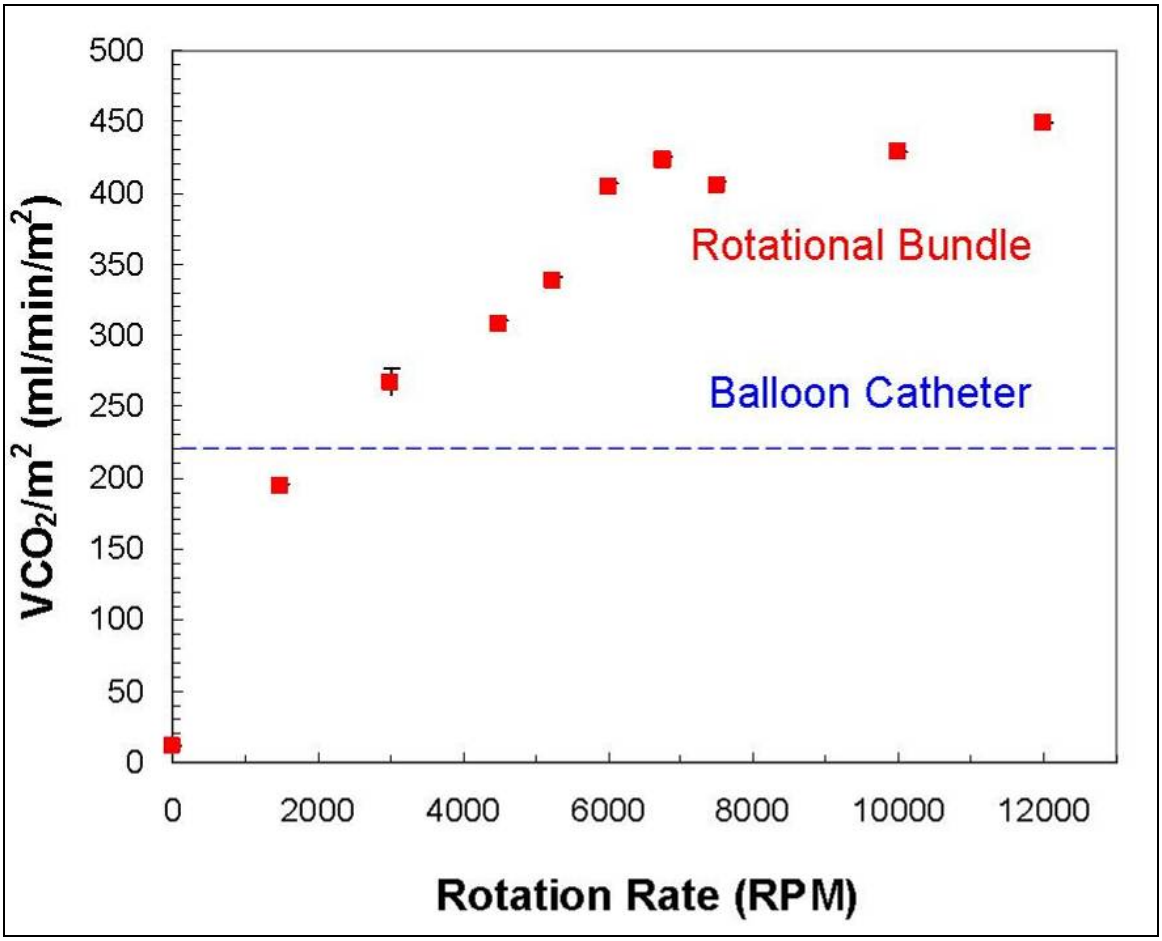

Figure 2-9: RP VCO_2 as a function of RPM [44].

The plateau indicated that active mixing by bundle rotation produced a similar effect on fluid particles when the rate was 7,000 RPM or higher. Particle image velocimetry (PIV) was performed by a lab post-doc to investigate the velocity fields surrounding the catheter during operation. The measurements showed the rotating bundle to generate secondary vortical flow patterns, or Taylor-like vortices, in the fluid that would enhance radial convective mixing with rate. However, no data or observations were obtained to directly explain the plateau of gas exchange. One hypothesis was that the vortices were not the principle mechanism for gas exchange enhancement but rather the penetration of fluid in the vortical flows into the fiber

bundle. As rotation rate increased, the intensity of vortices increased thus increasing fluid penetration and introduction of unprocessed fluid into the bundle. At higher rates, significant centrifugal and viscous forces may have been generated by the bundle that offset penetration into the interior bundle layers, and thus inhibited any further gas exchange enhancements. Detailed CFD analyses to understand the fluid mechanics at the higher rates were planned but eventually disregarded as parallel studies with the impeller concept showed promising potential.

Overall gas transfer rates between the rotational bundle and Hattler Catheter remained similar despite the increased efficiency. The corresponding rates for V_{CO2} for RP versus balloon catheter were 45 ml/min and 39 ml/min respectively. This was directly accounted for by the reduction in available surface area between the rotational catheter and balloon catheter (0.10 m^2 vs. 0.17 m^2). Thus, the rotational bundle concept provided greater CO_2 removal per unit area of HFM but was counterbalanced by the reduced surface area needed to meet size requirements.

Micro-bubble formation occurred as a result of material properties of the HFMs. The HFMs used in all prototypes were microporous permitting oxygen to bubble into the fluid when a transmembrane pressure differential was created at high RPM. A remedy for preventing the bubbles was needed in order to test the concept *in vivo*. Note, fibers proposed for use in commercial catheters would be coated or made of a composite material to inherently prevent the bubbles from leaking into the blood. The design solution incorporated a resistance valve in series in the sweep gas circuit prior to the inlet to lower the gas pressure throughout the bundle so that reduced local water pressures would still be large enough to avert micro-bubble forming pressure differentials. Figure 2-9 displays results of testing the resistance valve. The red data represented control VCO_2 in which the valve was absent and fluid pressure within the test section was raised to prevent micro-bubbles. Data in green displayed the effect of micro-bubbles on VCO_2 when the

test section fluid pressure was lowered to physiological pressures. Lastly, blue data represented samples taking at low water pressures with the presence of a sweep gas inlet resistance. The alignment of control and inlet resistance data showed micro-bubble formation to be eliminated at physiological pressures.

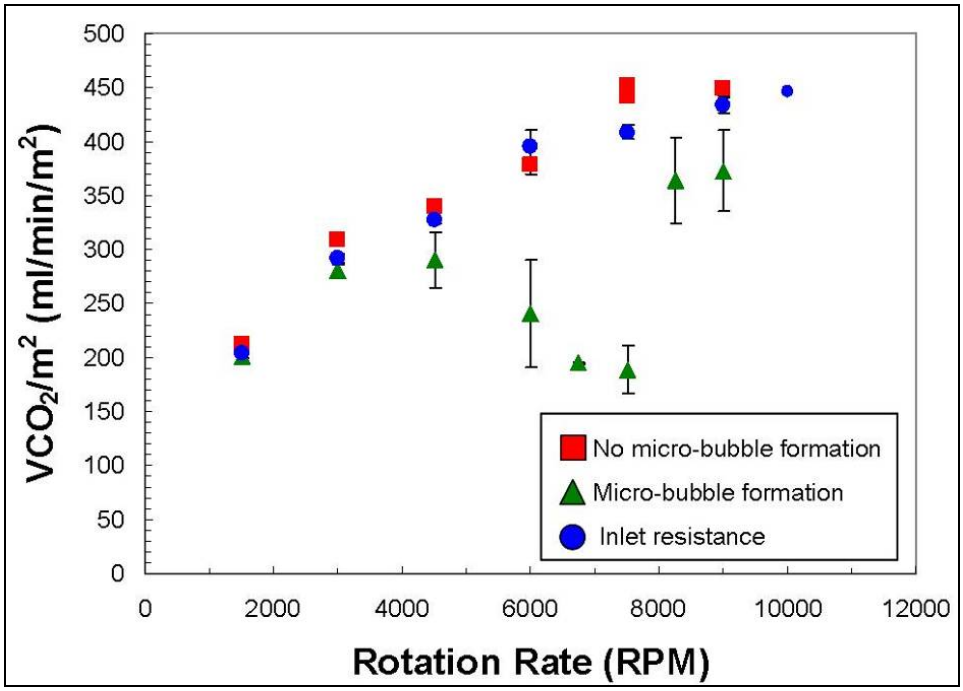

Figure 2-10: Micro-bubble influence on RP VCO_2 and design countermeasure.

An explanation for the trend displayed by the micro-bubble gas exchange (green) data was reasoned using parallel visual observations during the experiment. At 3,000 RPM, micro-bubbles were not observed within the test section and it was assumed that local water pressure had not decreased to levels permitting oxygen bubbling. This explained the similarity in efficiencies between all data. From 4,500 to 7,500 RPM, micro-bubble formation was also not visualized but the data displayed a large decrease in efficiency which was minimal at 7,500

RPM. It was hypothesized that the range was a transition in which bubbles began to obstruct the fiber pores and either remained or were slowly released, and thus incapable of visual perception. The pore obstruction possibly increased the boundary for CO_2 diffusion into the lumen and thus reduced efficiency. At 8,000 and 9,000 RPM, micro-bubble formation was noted within the test section. The transient release of bubbles created a mass transfer resistance to CO_2 diffusion and therefore efficiency was still reduced from control. Bubble formation, however, had less of an effect than in the transition range since release of pore occupying bubbles again provided open pores for diffusion, unlike in the transition range.

2.3.2 Hemolysis

The generation of plasma free hemoglobin by the RP prototype was evaluated in two hemolysis experiments. Blood total protein levels (5.9 g/dL vs. 6.5 g/dL) as well as RBC fragility indices (0.44 ± 0.01 versus 0.38 ± 0.01) were comparable in the two tests[44]. Results are located in Table 2-5. Plasma free hemoglobin is displayed as a rate of increase in units of concentration per time. The rate of increase in plasma free hemoglobin was similar between RP catheter and IABP in test group 1 but was greatly increased for RP catheter over IABP in group 2.

Table 2-5: Hemolysis results[44].

Group	Total Protein (g/dL)	Fragility Index	Hct %	PFHB: RP (mg/dL-h)	PFHB: control (mg/dL-h)
1	5.9	0.44	33	40	38
2	6.5	0.38	37	109	22

The data provided evidence that the rotation of HFM bundle *per se*, did not attribute to high hemolysis generation. Test group 1 PFHB rates were nearly identical indicating hemolysis

generated by the rotational bundle was similar to the IABP cardiovascular device. The differing result of test group 2 suggested that there was an element of variability responsible for the exaggerated results. Variability between blood batches was not reasoned as the fragility index of test group 1 was higher than group 2 suggesting that hemolysis was expected to be greater in group 1. This was confirmed by control PHFB rates between the two groups. The inflated group 2 test PFHB was then a result of variability between rotational bundle prototypes. The effect was not surprising since the prototypes were in early developmental stages with regards to blood-contacting rotational components (i.e. seals and lubrication). An example of the variability is depicted in Figure 2-11 where thrombus accumulation greatly differed on seals of even the same prototype. Seal function between prototypes therefore may have been responsible for the varied results. In conclusion, the tests revealed that the concept of rotating a HFM bundle was a feasible active mixing mechanism in regards to blood biocompatibility and warranted further investigation and advancements of the concept.

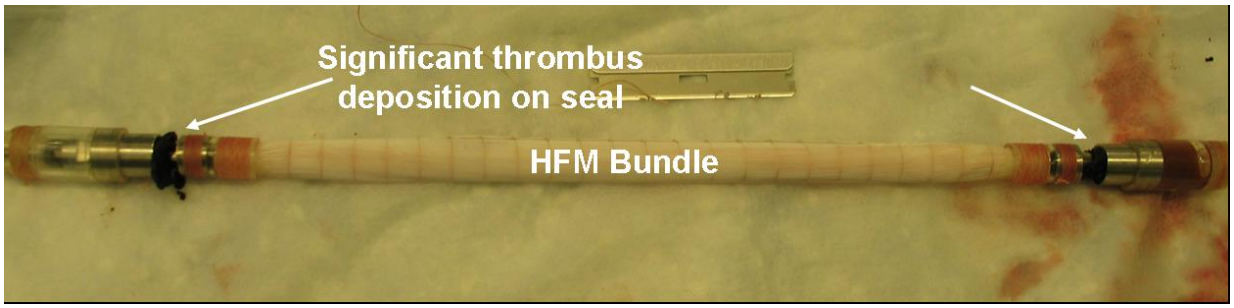

Figure 2-11: Thrombus disparity between RP seals.

2.3.3 Safety Cage and Implantable Prototype

The initial implantable prototype, RPI-1, was evaluated in a calf model but the design was unacceptable due to several factors. The first noted shortcoming was an underestimation of device size. The prototype exceeded targeted insertion size by 3 Fr as a direct consequence of the additional size needed to insert a safety cage within an insertional sheath. As a result, the changes to reduce the overall prototype diameter were initiated.

The rigidity of the RPI-1 catheter also proved to be a quality that prevented operation. Necropsy of the calf revealed a severe bend in the vasculature leading from the jugular vein to the superior vena cava. An example of prototype configuration in the tortuous vasculature is shown in Figure 2-12 (note: *in vivo* fluoroscopy image of impeller prototype). Prototype navigation through the bend exerted damaging stresses on tubing and drive shaft components. Furthermore, operating the device through the bend aggravated the condition causing prototype failures and leading to efforts of making the drive shaft and bundle tubing more flexible.

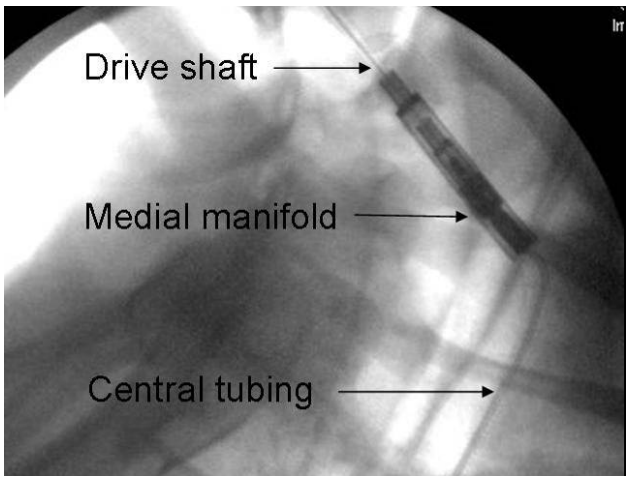

Figure 2-12: Prototype configuration in bovine vessel.

Lastly, the safety cage was shown to be inadequate for the design. The cage was vulnerable to point forces during the *in vivo* experiment that shifted the cage into the bundle causing fibers to entangle and tear. Figure 2-13 shows an example of the failure.

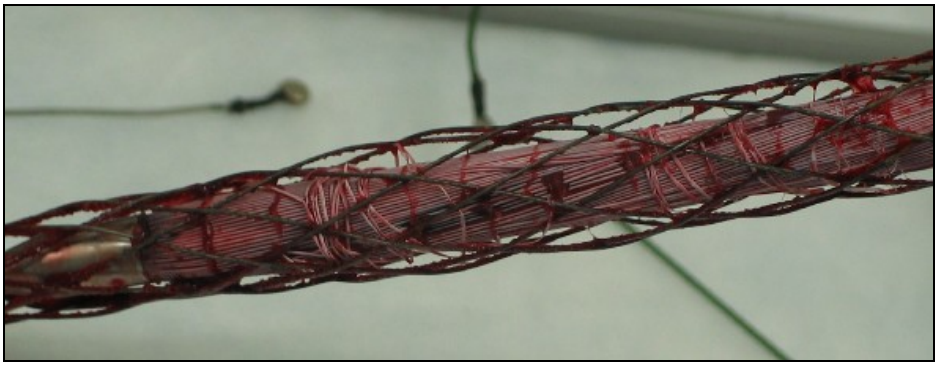

Figure 2-13: Displacement of safety cage resulting in critically damaged HFM bundle.

RPI-2 was fabricated to address the deficiencies of RPI-1. It became apparent that the catheter would unlikely operate effectively and the task of developing an adequate safety cage was tremendously challenging in itself. The prototype was tested in the tortuous loop to observe whether viable rotation and protection could be realized. Curvature of the test section coupled with the HFM bundle length and thickness prevented rotation of the device. The catheter configuration required much more torque from the servomotor than was available. Additionally, the huge question concerning vessel wall protection remained. A rotational bundle catheter required a safety cage that could remain concentric with the bundle through vessel curvature to avoid bundle contact. The volume occupied by the catheter during insertion dictated cage materials to be very thin in order to remain under 25 Fr, making the materials vulnerable to displacement under an applied force. The predicament presented an enormous design task, and

rotational bundle development ceased as the impeller concept showed to be a more promising candidate.

2.4 CONCLUSIONS

Actively mixing fluid through rotation proved to be a concept that enhanced mass transfer over the pulsating balloon catheter. Gas transfer efficiency in water was doubled from 230 ml CO_2/min/m^2 of the Hattler Catheter to 450 ml CO_2/min/m^2 of the rotational catheter. The design criterion of 25 Fr insertion size, however, diminished available surface area to 0.1 m^2 in comparison to 0.17 m^2 for the pulsating balloon catheter. This resultant loss caused the overall CO_2 transfer rates for both devices to be similar, roughly 40+ ml CO_2/min in water.

Hemolysis studies were performed on the bench to evaluate rotational bundle biocompatibility with blood. The rotation generated a PFHB rate (40 mg/dL-h) comparable to the clinically used Datascope IABP (38 mg/dL-h) and warranted further development of the rotating bundle catheter. A second hemolysis test was performed but the results were misrepresented under the hypothesis that seal heating and lubrication technique were contributing to hemolysis generation disparity between prototypes.

Development of the rotating bundle catheter proceeded and gas exchange data was pursued in an *in vivo* model with an implantable catheter. The data was not obtained but important information was gathered from the study nevertheless. Design changes were initiated to improve device flexibility, safety cage function, and insertional requirements.

A loop was fabricated to ensure that the improved implantable catheter could perform in tortuous vasculature that was observed in the *in vivo* study. Complications with rotating a bundle through curvature became more apparent, and requirements for an effective safety cage further substantiated the inherent challenges.

Studies were being performed in parallel with the rotating bundle catheter that featured a respiratory assist concept devoid of a safety cage. Preliminary studies showed that the design was a viable solution for operating anfractuous vasculature. The concept, the impeller catheter, is the focus of Chapter 3.

3.0 INTERNAL IMPELLER CATHETER

The second rotational concept to actively mix blood was the impeller catheter. Development began as rotational bundle studies revealed challenges concerning mechanical operation and functional safety cage design in a curved vessel environment. The impeller catheter provided improvement by utilizing the HFMs as a protective structure. Figure 3-1 displays the concept. The catheter incorporated an internal impeller capable of rotating at 20,000 RPM to impart fluid motion and expel fluid outwards radially. The benefit of increasing relative velocity of blood to fibers was still accomplished while an inherent safety structure was already present.

Concept evaluation was approached differently than the rotational bundle and only implantable prototypes were fabricated. Gas exchange tests were first performed to evaluate CO_2 removal efficiency. The tests were further subdivided to analyze the effects of impeller geometry on gas exchange in both the standard DI water solution and a blood representative viscous solution. Tortuous loop tests were implemented in early stages to ensure mechanical operation in severe bending environments. The prototype was tested in a calf model but design revisions were necessary to successfully complete *in vivo* evaluation. The prototype was improved and fatigue tests were conducted in bovine blood to assess the effectiveness of a saline seal purge. Following, the catheter was tested in four acute calf studies to examine gas exchange between

different impeller geometries. The design logic, research approach, and results are discussed in the following chapter.

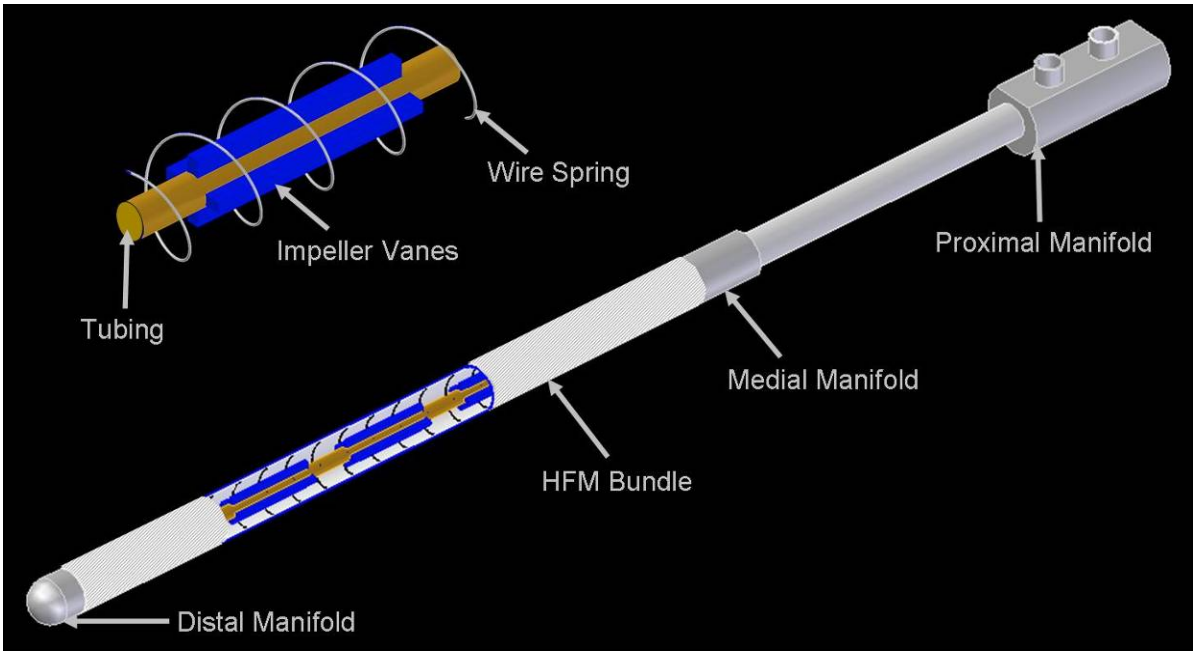

Figure 3-1: Internal impeller catheter concept.

3.1 DESIGN AND FABRICATION

An implantable catheter was developed from the start for concept evaluation. The prototype was designed so that impellers could be easily interchanged to rapidly evaluate impeller geometry. An application of epoxy to fix manifolds to the bundle was all that was required to take the prototype from bench to implant. Two design modifications were made to the catheter following

an initial set of implant failures. The design, materials used, and fabrication of the two prototypes are discussed in the section.

3.1.1 Prototype Designs

Implantable prototype 1: IP-1

The impeller PRAC (IP) concept required the bundle to enclose an internal rotating impeller and was achieved by forming HFM fabric around a stainless steel spring fabricated in-house. A 5 mm diameter cavity existed within the spring to create a hollow bundle module for the impeller to reside. The spring served as both a backbone to support fibers and as a barrier to shield from vanes located on the impeller. The support was secured to medial and distal manifolds and stretched to provide ample spacing for fluid passage. Celgard ARX30-240 hollow fiber membrane fabric was used. Characteristics of the HFMs and bundle are located in Table 3-1.

Table 3-1: HFMs (left) and impeller bundle (right) characteristics.

ARX30-240 HFM			**Impeller HFM Bundle**	
Material	Polypropylene		Bundle Length (cm)	30
Outer Diameter (μm)	300		Outer Diameter (mm)	8
Inner Diameter (μm)	240		# of Fibers	250
Average Pore Size (μm)	0.03		Fiber Layers	4
Porosity (%)	40		Wefts	none removed
Fibers per Inch (FPI)	54		Surface Area (m^2)	0.07

The sweep gas pathway for IP-1 was identical to the rotational bundle prototype. Oxygen gas was introduced into the proximal manifold and directed through the bundle. The distal manifold redirected exhaust gas back through the impeller tubing towards the proximal exhaust

port. Design calculations were performed to ensure an appropriate flowrate of 3 LPM through the prototype as described in section 1.5 and sub-section 2.1.1.

The selected material for the impeller was wire reinforced pebax tubing (#N98-TOL-664, New England Wire Technologies). The tubing was chosen from several samples based on tortuous loop test results discussed in Appendix A. Tubing characteristics are shown in Table 2-4. The impeller was connected to a drive shaft produced from an internal component of bi-directional 0.072" diameter shaft (#067N133C, S.S. White Technologies) that was coupled to the servomotor via the proximal manifold. The proximal manifold design was identical to that of the rotational bundle catheter.

Both the medial and distal manifolds contained a seal and two bearings to prevent blood intake and support concentric impeller rotation. Cut-away Solid Edge images of the manifolds are shown in Figure 3-2. Nitrile rubber rotary seals (#711800, Chicago Rawhide) were used. The seals accommodated shaft diameters of 0.110"-0.140" and had an outer diameter of 0.313". Each was modified in-house to an outer diameter of 0.250" in order to meet size specifications. The seals were also configured with a shielded, mini ball bearing (#35380815, MSC Industrial Supply Co.) possessing a 0.125" shaft diameter and 0.250" outer diameter. Fluid-side vespel material bearings were designed into the manifold housings adjacent to the exterior seal face for additional impeller stability. The material bearings were 0.5" in length with inner diameters of 0.113". The diameter created a 0.0005" clearance between the impeller and bearing wall.

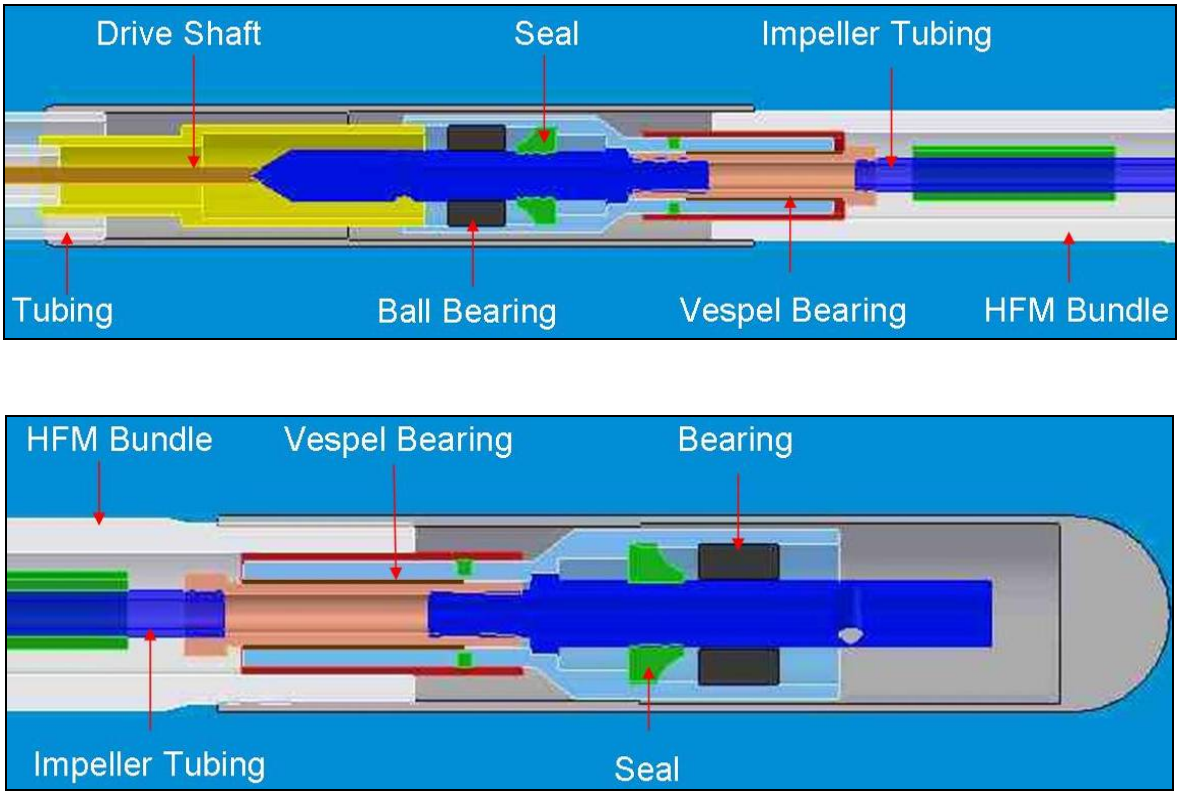

Figure 3-2: Impeller catheter medial manifold (top) and distal manifold (bottom).

Tortuous loop tests in Appendix A revealed that ½" length vane units with ½" spacing were sufficient to attain desired impeller flexibility. The vane units evaluated in the impeller catheter are shown in Figure 3-3. A cylindrical blank was made as a control and is not displayed. The paddle and axial units were fabricated in-house. Axial units were produced by turning static mixers (#04667-18, Cole Parmer Instrument Co.) on a lathe to a 0.152" outer diameter. A post-doc pursed the design of the other vane units. The process focused on reproducing known geometries rather than designing from in-depth theoretical approaches. "The design of turbomachinery has traditionally been highly experimental with simple theories only able to predict trends" commented Frank White[48]. Our design process was pursed experimentally as well since the understanding of the geometries was in preliminary stages and vane units could be

fabricated and tested in a cost-effective and timely manner. The units were produced by SLA rapid prototyping at the University of Pittsburgh Swanson Center. 2-flat, 4-flat, sawtooth, paddle, centrifugal and cone were developed as radial units. The RAX vanes comprised a combination of radial and axial geometries thought to assist in carrying fluid to the radial blades of the unit. All units had inner diameters of 0.084", outer diameters of 0.156", and lengths of 0.5".

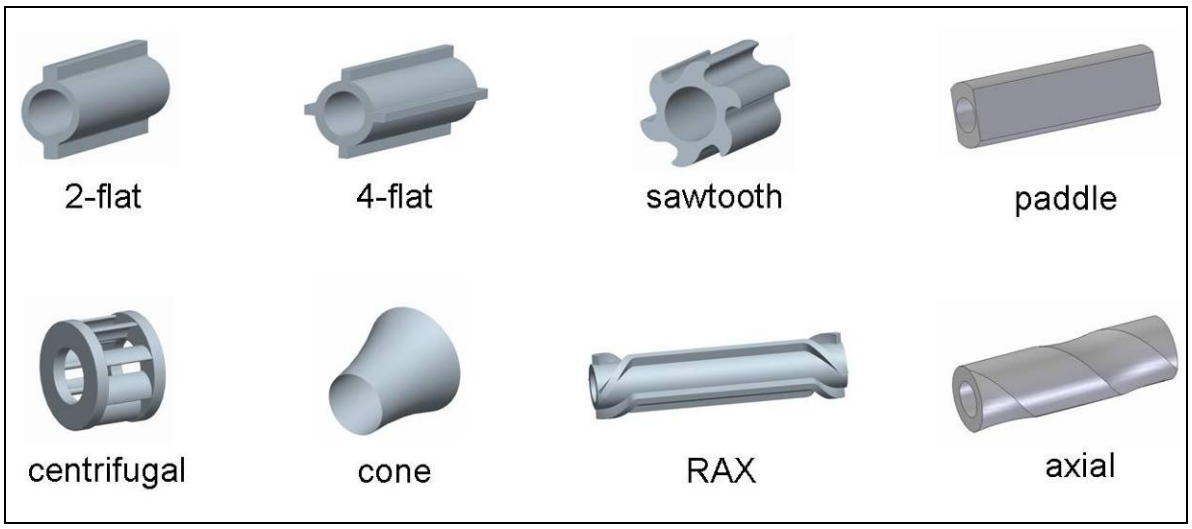

Figure 3-3: Impeller unit geometries.

Implantable prototype 2: IP-2

The evaluation of IP-1 in an animal model revealed mechanical failures of the impeller tubing. Prototype dissections showed accumulations of paste-like blood constituents in the external material bearings that were hypothesized to cause variations in friction between the two bearings, ultimately resulting in the tubing failure. A heparinized saline purge of the seals and exterior bearings was implemented to remedy the problem. The purge benefited the device three-

fold by: impeding blood penetration into the vespel bearings, preventing direct blood contact with the nitrile seals, and removing friction-generated heat from the seals.

Orifices were drilled into the medial and distal manifolds to deliver the saline to the exterior face of the seals and flush through the vespel bearing annulus. Two 304 stainless steel hypo tubing lines (#HTX-25R-24, Small Parts Inc.) with IDs of 0.010" and ODs of 0.020" were connected to the manifolds and laid through the exhaust tubing and proximal manifold to deliver saline. Reich and Gates suggested that a saline pressure of 200 mmHg was adequate to prevent blood seepage between a shank and seal[49]. Using this as a guideline the flowrate of saline through a single bearing to generate the pressure standard was calculated to be 12 ml/hr (Appendix B.2). The minimal flowrate was used in all prototype studies. Note that the part design was attributed to fabricator Brian Frankowski.

A concurrent effort was undertaken to improve the impeller tubing strength. Heraues Vadnais Inc. was contacted to develop a stainless steel coil (#HVT18642-01) for the impeller tubing. The coil consisted of 4-filar units that served to individually distribute torque loads. The coil was made to dimensions of 0.060" ID and 0.083" OD from 0.010" 304 stainless steel wire wound in a clockwise direction. Fundamentally, the impeller tubing was a hollow flexible drive shaft and could transmit higher loads than the plastic tubing. Pebax heat shrink tubing (#P2-140-006-CLR, Cobalt Polymers) with a wall thickness of 0.006" was applied to the coil in-house to produce the finalized, sealed tubing used in prototypes. The impeller was tested in a crude torsion testing apparatus, shown in Figure 3-4, to compare against other candidate tubings. The coil impeller managed much larger torsional deflections prior to failure and was therefore integrated into the IP-2 prototype.

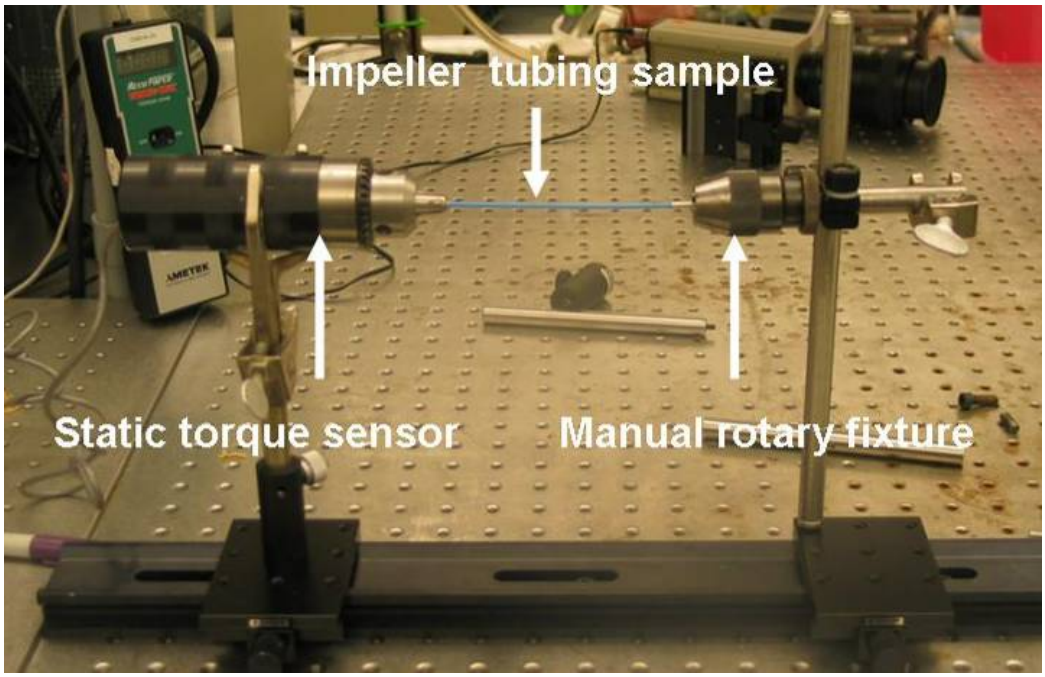

Figure 3-4: Torsion testing apparatus.

3.1.2 Fabrication

Manufacture of impeller catheter prototypes was performed by the fabricator. Most materials were identical to rotational prototype production. Important additions included the impellers and external bearings. WaterShed 11120 resin was used for impeller unit manufacture. The material was compatible with SLA prototyping and also resistant to water adsorption swelling. Limited clearance within the HFM bundle cavity necessitated the water resistant property. The external material bearings were made from Dupont vespel; this material had demonstrated application in use as a low wear material bearing. Drive components, medial and distal manifolds were fabricated from 316 stainless steel on a Hardinge lathe. The acrylic proximal manifold was directly substituted from the rotational bundle catheter. Inlet and exhaust tubings were made of

polyurethane plastic. Component mating was accomplished using the 2:3 polycin to vorite epoxy or Permeatex clear RTV silicone adhesive sealant. Mechanical drive parts were connected using silver solder.

3.2 EVALUATIVE TESTS

Impeller prototype feasibility was evaluated on the bench and followed by studies in a bovine model. Gas exchange tests of the IP-1 prototype were conducted *in vitro* to assess CO_2 removal efficiencies with the various impeller units. The prototypes were tested in the standard DI water and a viscous solution similar to blood in order to provide insight regarding impeller geometry performance. The initial failure of IP-1 in the animal prompted incorporation of a heparinized saline purge which was assessed by testing prototype fatigue in a blood loop. Successful saline purge results lead to the evaluation of IP-2 *in vivo* to increase understanding of gas exchange ability. The section will detail the methods used to evaluate the impeller concept catheter.

3.2.1 Gas Exchange

Gas exchange testing evaluated the affect of impeller geometry on CO_2 removal efficiency. The nine differing impellers were tested in the IP-1 prototype. The testing circuit and methods were nearly identical to those of the rotating bundle in sub-section 2.2.1. The primary alteration to the methods was extending testing to a viscous solution. The viscous solution test evaluated the interplay between the impeller transmitting motion to the fluid versus the bundle impeding fluid

velocity. A higher viscosity solution, such as blood, transmits fluid motion better thus increasing relative velocity to fiber, whereas the bundle region impedes fluid motion and decreases relative velocity. A 0.4% w/w concentration of carboxymethylcellulose (CMC) sodium salt (#C5678-500G, Sigma-Aldrich Inc.) and DI water was interchanged with homogenous DI water to test prototypes in both solutions. The viscosity of the CMC solution was measured at 37 ˚C during each test using a capillary viscometer (#150, Cannon Instrument Co) to ensure that the viscosity remained in a range of 2.5-2.7 cP. CMC was used as the solution thickener because a minute concentration could be added to water without altering the gas solubility properties.

Cavitation and micro-bubble phenomena were not observed with the impeller catheter and therefore the fluid pressure within the test section was maintained at 10 mmHg for all tests. Sweep flowrate was kept at 3 LPM to facilitate the sweep gas independency criteria described by Federspiel and Hattler[42].

3.2.2 Impeller Fatigue

Experiments were performed to test the effectiveness of the heparinized saline purge prior to implementing in IP-2. The tests were conducted in a bench blood circuit to identify whether blood infiltration and subsequent accumulation in the external bearings was responsible for the torsional failures witnessed in the initial *in vivo* study. Mock devices consisting of only the rotational components were first tested, and results warranted further testing with full prototypes. Two prototypes were tested in the final fatigue study. The first was an IP-1 absent of the saline purge that served as the test control; the second was the IP-2 prototype with saline purge system.

Both prototypes were placed in parallel ⅞" test sections within the blood circuit. Blood was re-circulated through each test section at a flowrate of 1.5 LPM and maintained at 37 ˚C. Two liters of blood (Heparinized bovine blood, Hemostat Laboratories) were used in the circuit. The blood was characterized at the beginning for ACT and fibrinogen content. A schematic of the blood loop is shown in Figure 3-5.

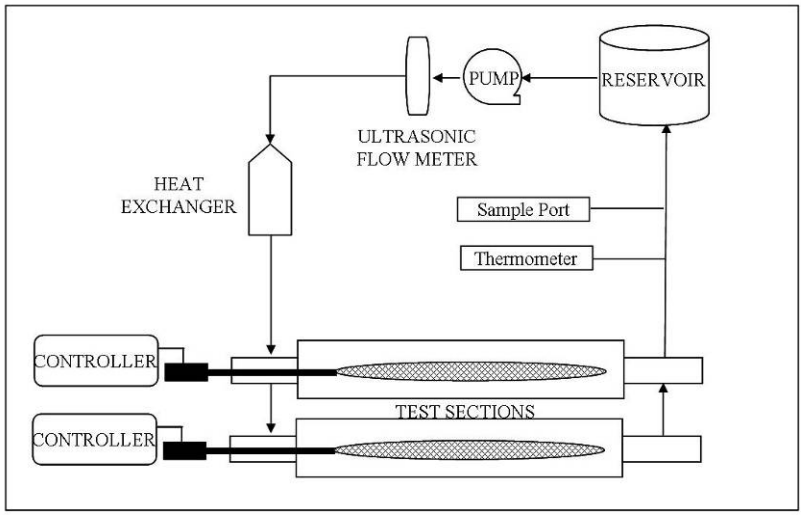

Figure 3-5: Saline purge fatigue test circuit.

Saline was pumped into each IP-2 bearing site at a flowrate of 12 ml/hr using a peristaltic pump. The drive consoles were programmed to record elapsed time and 1¼ amp fuses were installed into each. The fuses automated the system to shutdown upon failure and permitted the fatigue testing to be conducted overnight under no supervision. The prototypes were operated at a constant speed of 10,000 RPM for the test duration. Motor torque requirements and elapsed time were recorded. All equipment used for fatigue testing is described in Table 3-2.

Table 3-2: Fatigue test equipment.

Component	Model	Manufacturer
Blood	2 L heparinized bovine blood	Hemostat Laboratories
Ultrasonic flow probe	T110	Transonic Systems Inc.
Reservoir bag	Affinity Reservoir Bag #321	Medtronic Inc.
Blood pump	Biomedicus biopump BPX-80	Medtronic Inc.
Pump console	540 Bio-console	Medtronic Inc.
Pediatric heat exchanger	D1078	Medtronic Biotronics
Thermometer	Digi-sense type T thermocouple	Cole-Parmer Instrument Co.
Temperature pump	T/Pump TP-406	Gaymar Industries
Peristaltic pump	Masterflex C/L 77120-62	Barnant Company

3.2.3 Acute Animal Studies

Testing was transitioned from the bench to an *in vivo* environment to evaluate device performance in a physiological setting. All *in vivo* studies performed were acute studies with the objective of obtaining CO_2 exchange measurements in a bovine model. The three impellers that emerged from bench gas exchange characterizations (4-flat, RAX, sawtooth) were tested in IP-2. Prototype gas exchange was measured in two different vena cava positions. The first location was a position spanning the right atrium where longitudinal blood flow in the IVC and a cross-

flow into the right atrium were experienced. The second position evaluated the catheter solely in the IVC where only longitudinal flow past the device occurred.

All experiments were performed at a University of Pittsburgh animal facility possessing the proper staff and surgical equipment to provide full animal care. The surgical procedure and testing protocol were authorized by the University of Pittsburgh IRB. Calves weighing ≈ 100-125 kg were used in the experiments. The animal was fitted with a Swan-Ganz catheter and femoral pressure line following anaesthetization. Heparin infusion was administered per surgeon discretion into the femoral vein. Guidewires for device insertion were laid through the jugular vein and femoral vein using a 2-cuppped magnet system. The jugular vein was exposed and an incision was made. Upon insertion the IP-2 prototype was extended through the jugular vein into the vena cava to situate in either of the two locations described previously.

All equipment used in the gas circuit for bench exchange characterization was used (refer to subsection 2.2.1). CO_2 removal efficiency was calculated in accordance to equations (2) and (3). The purge flowrate was 12 ml/hr of 1:50 heparin to saline solution. The femoral blood pCO_2 was maintained in the range of 45-55 mmHg by adjusting ventilator settings.

Testing protocol began when calf femoral pCO_2 stabilized within the requested range. The prototype was tested over the full RPM range of 200-20,000 RPM in a randomized fashion. CO_2 exhaust concentration, sweep gas flowrate, sweep gas pressure drop, and torque were acquired at rates of 200, 5,000, 10,000, 15,000 and 20,000 RPM. Each data point was obtained at least twice to ensure repeatability. The protocol was initiated in both vena cava locations before a different impeller prototype was inserted. Calve arterial and femoral pressures were monitored and plasma free hemoglobin samples were obtained through the course of testing. Following the experiment, a necropsy was performed to view the vasculature. Prototypes were later dissected

on the bench to observe any thrombus formation, failure sites, and seal wear/ appearance. A concise outline of the protocol can be read in Appendix C.

3.3 RESULTS AND DISCUSSION

3.3.1 Gas Exchange

Nine impeller geometries were evaluated for CO_2 removal efficiency. Maximum gas exchange occurred at the peak rotational rate of 20,000 RPM. Figure 3-6 displays prototype characterization plots of VCO_2 versus RPM in both testing solutions. Maximum efficiencies for all geometries are listed in Table 3-3, and it is observed that the 4-flat, RAX, sawtooth, and 2-flat geometries performed similarly. It is hypothesized that the centrifugal geometry had a lower efficiency compared to other radial geometries since the ends were enclosed and fluid could not penetrate the vanes as well as open-ended geometries. The cone geometry was the worst performing unit, even when compared to the cylindrical control. The tapered end caused the cone unit to have a lower average linear velocity at the surface. This transmitted less momentum to fluid particles and was likely the reason for the cone underperforming even the control.

The effect of increased viscosity was consistent between geometries. A fluid viscosity in the range of 2.5-2.7 cP decreased gas exchange by approximately 20-30% at 20,000 RPM when compared to water. The reduction was due to the increased drag forces on fluid particles as they

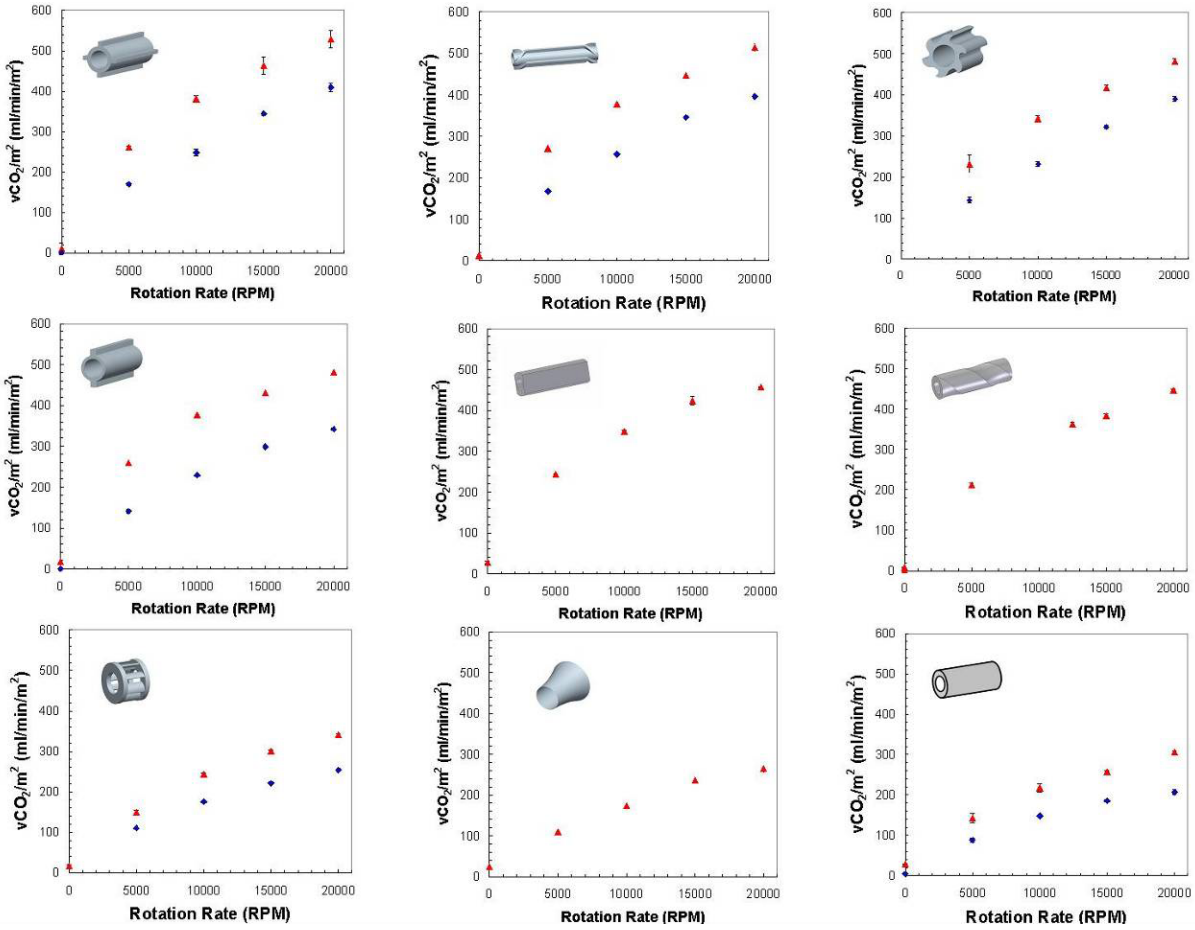

Figure 3-6: CO_2 removal efficiency plots according to impeller geometry.

Blue: Viscous solution, Red: DI water.

Table 3-3: Maximum CO_2 removal efficiency corresponding to impeller geometry.

Impeller	VCO_2 (ml CO_2/min/m^2)
control	307 ± 3
4-flat	529 ± 21
RAX	514 ± 11
sawtooth	482 ± 6
2-flat	482 ± 3
paddle	457 ± 1
axial	446 ± 3
centrifugal	341 ± 2
cone	264 ± 10

traversed the HFM bundle. Velocity of a fluid flowing through a porous medium can be theorized according to Darcy's Law which states:

$$\vec{Vo} = -\frac{k}{\mu}(\nabla P - \rho\vec{g}) \qquad (4)$$

where $\vec{Vo}$ is the velocity field vector, k is permeability, μ is viscosity, ∇P is the pressure gradient, ρ is fluid density, and $\vec{g}$ is the force of gravity. The fluid velocity through the medium is indirectly proportional to the viscosity and fluids with higher viscosities will exhibit lower relative velocities to fibers at a given RPM rate, thus inhibiting boundary layer reduction. This was observed between the two solutions per the reduction in efficiency.

CO_2 exchange in blood was approximately 20-40% greater than in water when the Hattler Catheter was evaluated[50]. The blood viscosity resembling solution provided a reference for estimating impeller prototype efficiency enhancement in blood by incorporating relevant viscous effects into the system. The expected increase in efficiency due to blood CO_2 capacity was similar to the magnitude of efficiency reduction caused by viscosity. Therefore, it was hypothesized that removal efficiencies *in vivo* would achieve rates similar to those observed in standard DI water.

A common empirical mass transfer correlation for analyzing oxygenator gas exchange was determined from an analogous heat transfer correlation for perpendicular tube bank flow and is in the form $Sh = a\,\mathrm{Re}^{b}\,Sc^{1/3}$, where Sh is the Sherwood number, Re is the Reynolds number, and Sc is the Schmidt number[51-53]. The coefficients a, b are dependant on fiber bundle geometry and are determined experimentally, however, coefficient b can be loosely approximated as b=0.5. If the velocity term in the Reynolds number is assumed proportional to rotation rate, VCO_2 can be compared to $RPM^{1/2}$ to assess mass transfer of the IP prototype. Figure 3-7 shows the

correlation for all nine impellers tested on the bench. The linear relationship between VCO_2 and $RPM^{1/2}$ indicated that the CO_2 driving gradient for gas exchange at higher RPM was not reduced, and therefore was not likely an explanation for the observed leveling trend of gas exchange. The trend was not investigated further; however a second hypothesis to explain the plateau was that specific fiber layers or fiber regions within the bundle were not fully utilized in exchanging gas due to an inefficient fluid mixing mechanism.

The outcome of bench gas exchange testing was to proceed with the 4-flat, RAX, and sawtooth impeller geometries to *in vivo* studies.

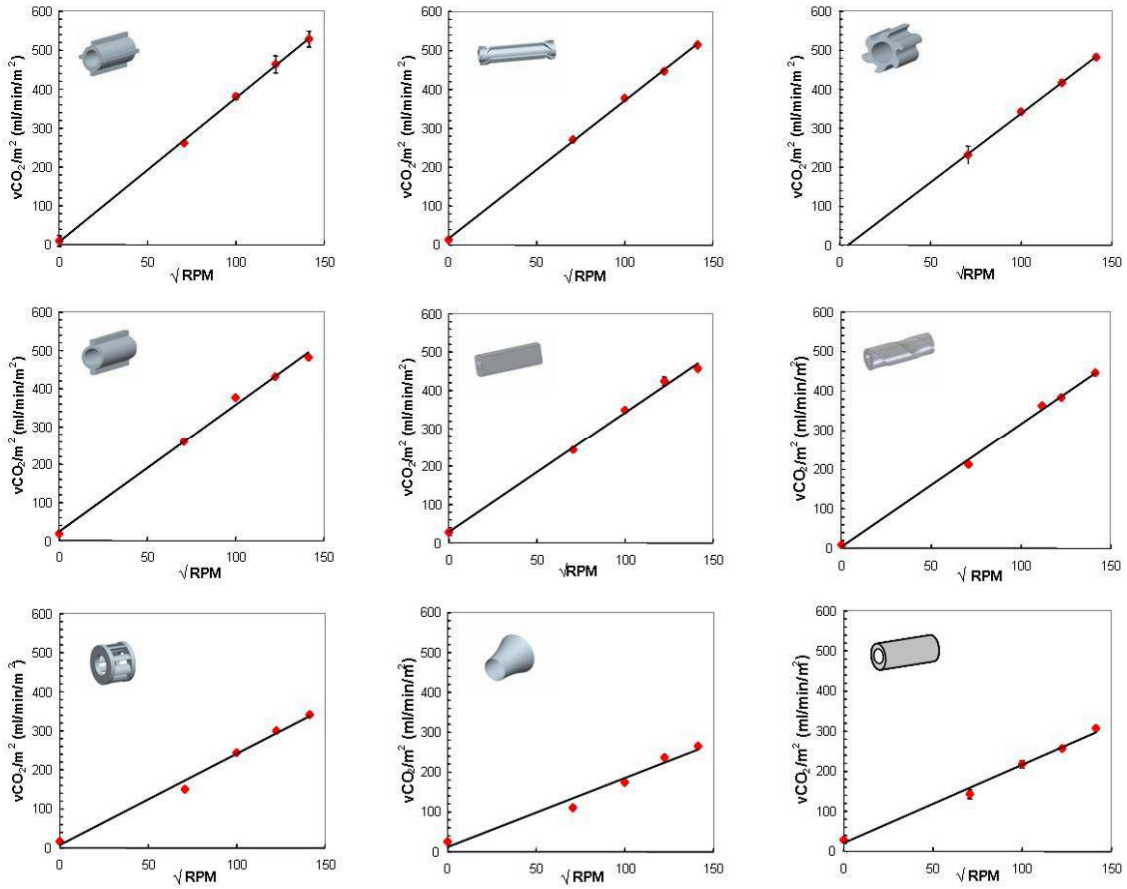

Figure 3-7: Impeller efficiency mass transfer correlation.

3.3.2 Impeller Fatigue

Results of preliminary component and full prototype blood fatigue tests showed the saline purge to be an effective means for preventing torsional impeller tubing failures. In the full prototype experiment, IP-2 with saline purge was operated for 24 hours and did not show indication of potential failure. The prototype was shutdown willingly since the operating time far exceeded that necessary to complete an acute bovine study. The IP-1 control prototype without purge, however, failed two hours after the test start. A plot of motor current requirement versus elapsed time is shown in Figure 3-7. It is observed that the IP-2 prototype operated at a constant torque until test completion (recall motor torque is proportional to motor current). An increase in torque to failure is observed for the IP-1 control due to the build-up of blood constituents in the material bearings.

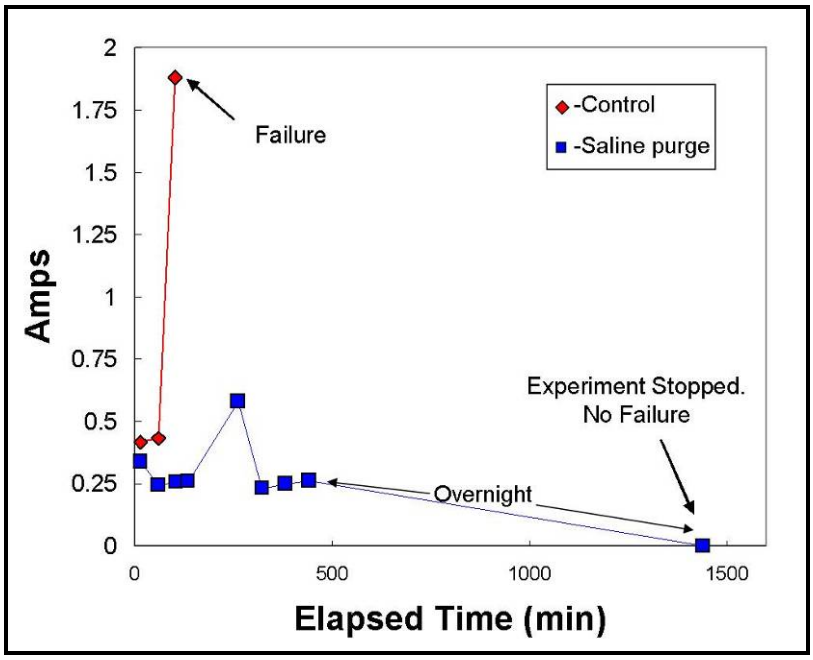

Figure 3-8: Effectiveness of saline purge in preventing impeller failure.

The blood accumulation was confirmed by dissecting the prototypes and examining rotational components. The build-up replicated observations of failed devices *in vivo* and is exemplified in Figure 3-8 (left). In contrast, the IP-2 prototype revealed seals and bearings free from blood contact as confirmed in Figure 3-8 (right). The saline purge was thus implemented into the implantable prototype for *in vivo* evaluations.

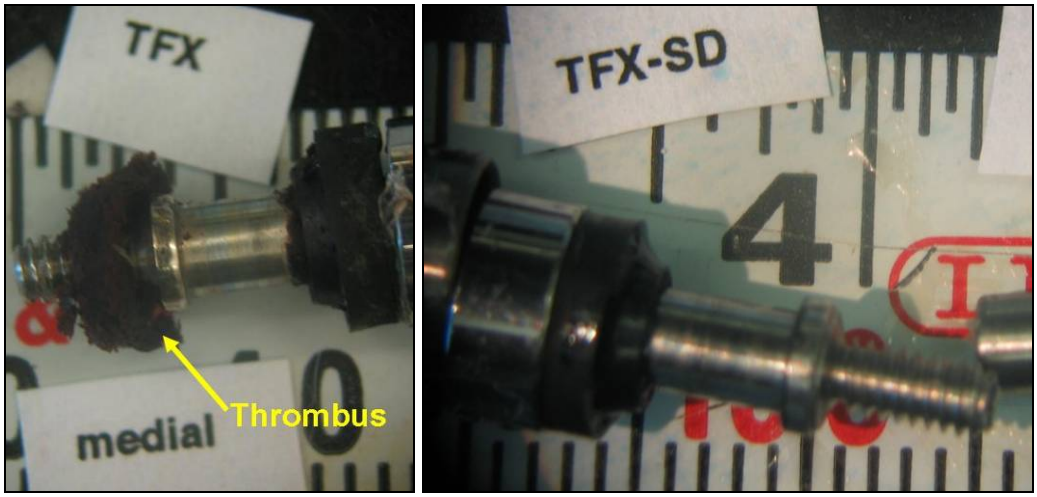

Figure 3-9: (Left) Seal thrombus observed in device without saline purge .

(Right) Clean seal in device with saline purge.

3.3.3 Acute Animal Studies

Initial bovine experiments revealed impeller catheter design shortcomings that consequently caused failures during testing. The concerns were addressed in the design of IP-2 and enabled successful gas exchange evaluation *in vivo*.

IP-1 impeller tubing failures occurred during initial tests. The tubing experienced non-uniform rotation between the medial and distal housings that created torsional stresses along the tubing length. Evidence of the stresses is shown in Figure 3-9(A) and 3-9(B). The combination of high-speed and torque caused the tubing to fail in two ways: either the tubing completely ruptured leaving a helical pattern in the direction of motor rotation, or the hollow tubing collapsed on itself with the same observed pattern. The pattern indicated a delay or complete seizure in impeller angular velocity in the distal manifold causing the tubing to overturn. The problem was remedied by both replacing the pebax tubing with the coil shaft to improve torque transmission and implementing the saline purge. Figure 3-10(C) displays intact impeller tubing of an IP-2 prototype following a successful *in vivo* test.

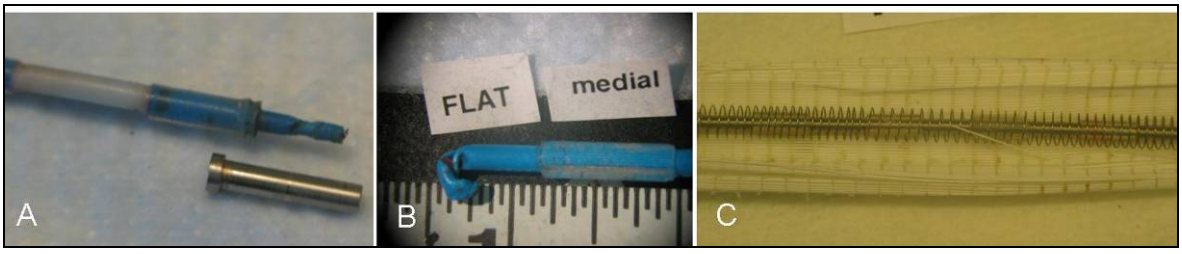

Figure 3-10: (A) & (B): Tubing failures due to excessive torsion.

(C): Intact coil tubing after a successful experiment.

Analysis of the external bearings of IP-1 after experimentation revealed an accumulation of blood constituents that augmented friction between impeller tubing and bearing. The bearing served as an undesired annulus for blood to travel through and contact the seal. Figure 3-10(A) indicates blood thrombus on the seal following an *in vivo* failure. The blood penetrated the external bearing housing shown in Figure 3-10(B) prior to contacting the seal. Shear stress

calculations on the blood within the bearings estimated a stress exposure of 5,000 dynes/cm^2 at 20,000 RPM (Appendix B.1). Paul et al. found the shear stress threshold for hemolysis to be 3750 dynes/cm^2 and 4250 dynes/cm^2 at exposure times of 1.4 and 0.425 seconds respectively[54]. The bearing shear stress level was likely causing hemolysis and contributing to the accumulation. The saline purge system was executed to create a fluid barrier and prevent blood from entering the bearing. Figure 3-10(C) displays a seal from an IP-2 prototype possessing the purge. The seal was clean of thrombus indicating successful fluid flushing.

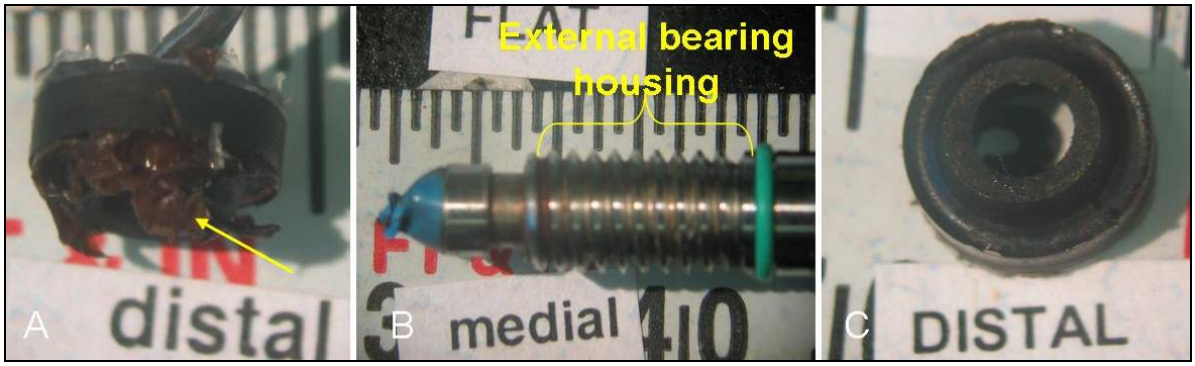

Figure 3-11: (A) Thrombus deposition on seal. (B) External bearing region. (C) Clean seal after successful *in vivo* operation.

Impeller catheter gas exchange data was obtained in four different calves using IP-2 prototypes. The results of impeller geometry influence match the trend identified in bench-testing. Figure 3-11 shows the maximum average CO_2 removal efficiencies for 4-flat, RAX, and sawtooth impellers. The 4-flat geometry produced the most favorable efficiency level and was found to be significantly higher than the sawtooth geometry. The corresponding *in vivo* removal rates were: 36 ml CO_2/min for 4-flat, 34 ml CO_2/min for RAX, and 33 ml CO_2/min for sawtooth.

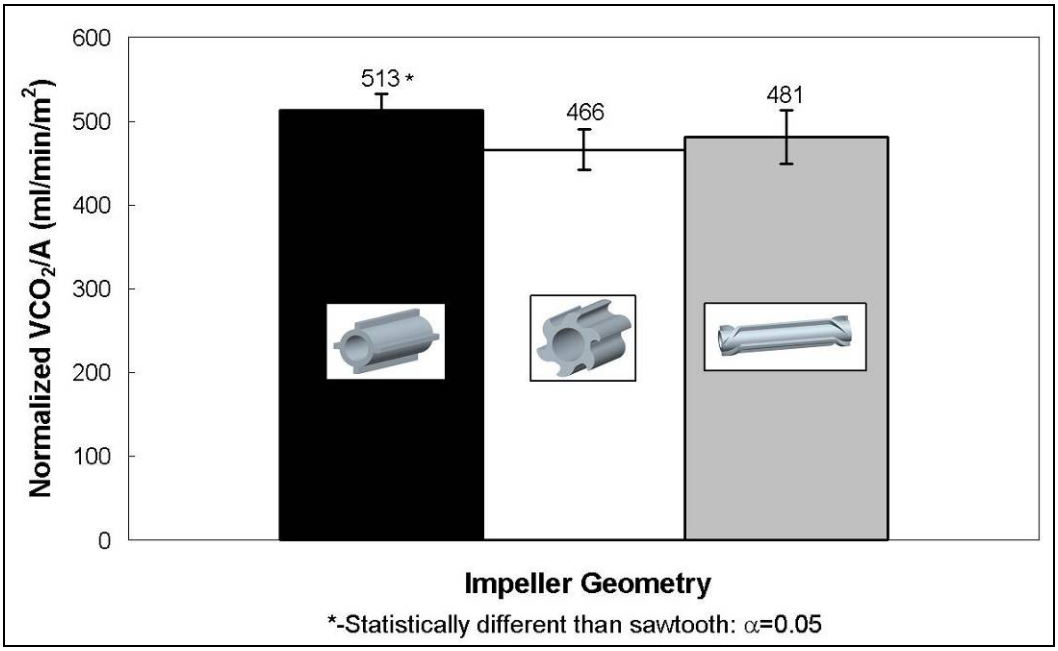

Figure 3-12: IP-2 average maximum efficiencies observed *in vivo*.

A typical plot of efficiency versus RPM is displayed in Figure 3-12. Gas exchange increased as a function of rotational rate. The slope for the IP-2, however, began to trend towards zero near 20,000 RPM indicating a maximum efficiency plateau. An inspection of all data did not show prototype location spanning the right atrium to be more beneficial in comparison to the IVC. The conclusion may be limited by the necessity to configure the prototype in vena cava positions avoiding severe tortuousness which may have exposed the catheter to the right atrium mixing in both intended locations.

Maximum removal efficiencies in blood were very similar to bench gas exchange results obtained using normal DI water. An increase in CO_2 removal over DI water was not observed in blood because the ability of blood to carry a higher CO_2 content was offset by the increased bundle drag forces and consequent reduction in relative fluid velocity resulting from a higher

fluid viscosity. Bench-testing of the impeller prototype in standard DI water provided an accurate prediction of maximum CO_2 exchange.

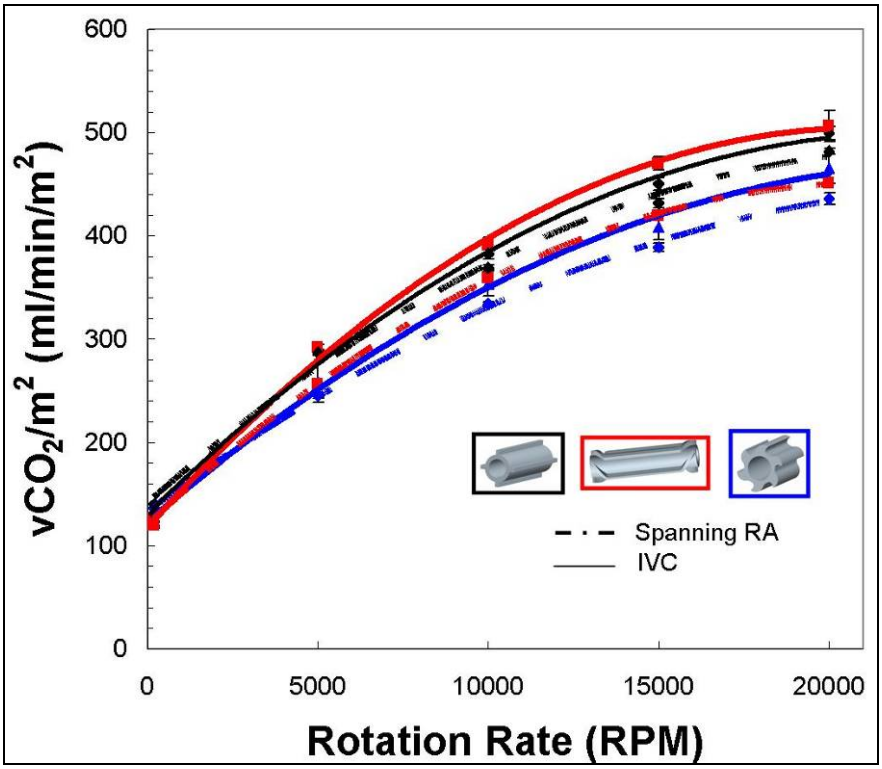

Figure 3-13: *In vivo* IP-2 efficiency plot.

Plasma free hemoglobin samples were measured during protocol but conclusions were difficult to draw since the aim of the experiments were to evaluate gas exchange. At least three prototypes were inserted per calve thus subjecting the blood to different impeller geometries and making it difficult to assess individual impeller blood biocompatibility. Data from two studies in which a specific impeller was evaluated over three hours is shown in Figure 3-13. The evaluations were performed following gas exchange testing. The 4-flat impeller at 10,000 RPM seemed to produce a constant level of hemolysis between 20-25 mg PFHB/dL whereas the RAX

impeller at 15,000 RPM appeared to generate an increasing rate. Whether the RPM rate or impeller geometry was accountable cannot be deduced. Appendix C.1 contains a plot of hemolysis versus elapsed time for all experiments. The prototypes appeared to generate consistent levels between 20-40 mg PFHB/dL that trend towards a constant or decreasing rate. Further conclusions cannot be drawn about the IP-2 hemolysis generation. A chronic *in vivo* experiment or multiple bench tests could be conducted in the future to fully understand impeller prototype hemolysis should the need arise.

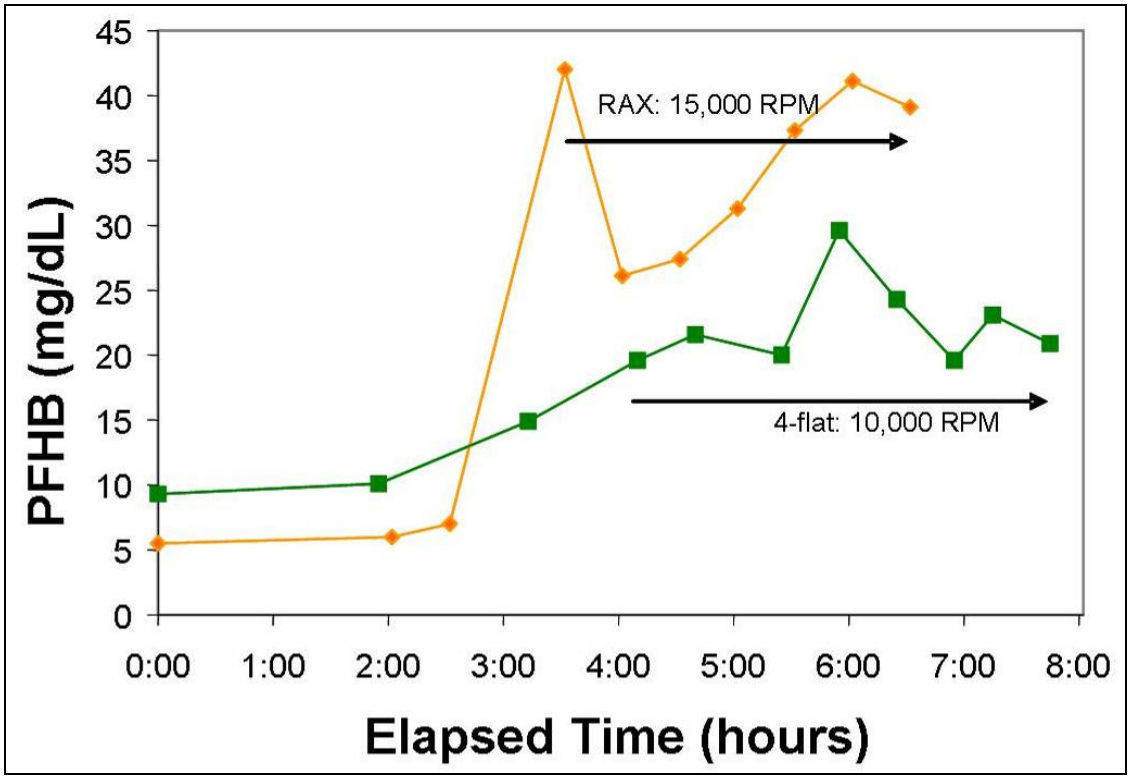

Figure 3-14: *In vivo* hemolysis generation for two impellers.

3.4 CONCLUSIONS

The impeller catheter proved to be more feasible than the rotational bundle. The design incorporated an element of flexibility that enabled functional operation in tortuous vasculature. Utilization of a stationary hollow fiber bundle as a protective structure against impeller-vessel wall contact was a further significant improvement. Finally, the saline purge provided a more biocompatible seal component where blood was prevented from contacting the frictional interface, a site for potential RBC injury.

The prototype was tested on the bench in two different solutions to examine the effects of solution viscosity. Nine impellers were observed to analyze the response of fluid mechanics to geometry. A maximum CO_2 removal efficiency of 529 ml CO_2/min/m^2 was observed in DI water corresponding to an 18% increase over the rotating bundle. Testing in a viscous solution revealed that the relative fluid velocity through the HFM bundle was impeded because of increased drag forces caused by the fiber medium. The leading geometries of 4-flat, sawtooth, and RAX proceeded from bench to acute *in vivo* studies.

Early *in vivo* studies exposed design deficiencies and the subsequent modifications integrated an impeller coil tubing and saline seal purge. The studies were performed in a bovine model in locations of the inferior vena cava and spanning the right atrium. A maximum average efficiency of 513 ± 20 ml CO_2/min/m^2 was obtained with the 4-flat impeller geometry. Vena cava position was not observed to substantially affect gas exchange. The impeller catheter was successfully carried through concept to functional prototype capable of testing in the tortuous vasculature of a calve model.

4.0 ROTATIONAL ENHANCEMENT CONCLUSIONS

An approach to producing a smaller respiratory assist catheter for percutaneous insertion focused on evaluating rotation as a means for active mixing. Rotation was an attainable mechanism to increase the relative velocity of fibers to blood over the Hattler Catheter in order to increase mass transfer to reduce catheter size.

The first concept developed utilized HFM bundle rotation to generate gas exchange. A bundle of 0.1 m^2 surface area was rotated at speeds approaching 10,000 RPM. A two-fold increase in CO_2 removal efficiency over the HC was observed with the device achieving a maximum efficiency of 450 ml CO_2/min/m^2 in standard DI water bench-testing. *In vitro* hemolysis studies to examine blood damage caused by the rotating bundle showed rotation to cause similar hemolysis to an intra aortic balloon pump, a clinically used cardiovascular device, and therefore was a practical mechanism to increase efficiency. An *in vivo* test and subsequent tortuous loop test with the prototype revealed that the speeds necessary to augment gas exchange were very difficult to realize in a tortuous environment. The limitation was further complicated by the need to develop a strong, flexible safety structure to protect the vessel wall from device contact. Steps were initiated to begin developing the second concept.

The impeller concept improved over the rotating bundle by including the HFM bundle as the protective structure against rotating components. The prototype consisted of a hollow bundle module within which an impeller rotated at 20,000 RPM to generate fluid mixing. The impeller catheter had a total HFM surface area of 0.07 m^2 and produced a maximum efficiency of 529 ml $CO_2/min/m^2$ in DI water. Nine different impeller geometries were analyzed overall. A saline purge was added to flush seals and external bearings of any blood intake. Three prototypes consisting of 4-flat, sawtooth, or RAX impeller geometries were tested in acute bovine studies. The maximum CO_2 efficiencies observed for the prototypes were 513 ± 20 ml $CO_2/min/m^2$, 466 ± 24 ml $CO_2/min/m^2$, and 481 ± 32 ml $CO_2/min/m^2$ respectively.

The impeller catheter enhanced *in vivo* CO_2 removal efficiency by 70% over the Hattler Catheter and confirmed the effectiveness of rotation. The device was capable of operating in tortuous vasculature while protecting the vena cava wall unlike the rotational bundle. The tradeoff in HFM surface area to reduce size however, handicapped overall CO_2 removal rates. Removal rate was ultimately higher in the HC because of its 2 ½ fold greater surface area. See Table 4-1 for an overview of catheter performances.

Table 4-1: Catheter performances.

Catheter	Surface Area (m^2)	*In vitro* Efficiency (ml $CO_2/min/m^2$)	*In vivo* Efficiency (ml $CO_2/min/m^2$)	CO_2 Removal Rate (ml CO_2/min)
Hattler	0.17	230	300	51
Rotating Bundle	0.10	450	NA	45
Impeller	0.07	529	513	36

The impeller catheter met the percutaneous insertion size requirement of 25 Fr. Progress was accomplished in developing a more efficient CO_2 gas removing device. Future work requires the development of different fluid mixing concepts or addition of bio-active components to the design. Concurrent research in the lab is focused on immobilizing carbonic anhydrase enzyme onto hollow fiber membranes. The enzyme catalyzes blood bicarbonate into carbon dioxide and has the potential to increase the fundamental CO_2 exchange driving gradient. Enhanced CO_2 diffusion into the fibers may increase gas exchange to the targeted levels of 75-85 ml/min and beyond. Integration of bio-active fibers and impeller catheter design may be the final step to successfully achieving all project objectives.

APPENDIX A

TORTUOUS LOOP COMPONENT TESTS

Mechanical failure of the rotating bundle prototype due to inflexibility during the *in vivo* bovine study required the central tubing to be replaced. The tubing substitute was applied to both the RPI-2 and IP-1 prototypes. Reinforced plastic tubing was requested from companies for the component. Tubing samples were tested and chosen on an experimental basis since directly designing tubing required knowledge of unavailable tube material properties and complex structural analyses of wire mesh structures. Testing samples provided a timely and cost-effective alternative. The following provides a brief discussion of the tests and results of component function in a tortuous environment. The tests were also beneficial for determining the length of impeller units to retain flexibility in the impeller prototype. Three tubings were tested in the tortuous loop setup to evaluate torque requirements, fatigue, and impeller length. The sample group is shown in Table A-1.

The tortuous loop test section is dimensioned in Figure 2-13 and shown in Figure A-1. The testing device was placed in the loop and water was circulated to provide a fluid environment. The test device was a "skeleton" impeller prototype in which tubing samples could be easily substituted. Testing was performed without a HFM bundle except in one instance to

evaluate the effect of the bundle decreasing bending radii. Torque was calculated by measuring the current into the drive system and converting by means of the motor torque constant.

Table A-1: Selected tubings for tortuous testing.

Manufacturer	Part #	Material	Mesh	Sealant Topcoat
(A) New England Wire Technologies	NEC00029	Clear Pebax 6333	40 AWG 304 stainless steel	NA
(B) New England Wire Technologies	N98-TOL-664	Blue Pebax	44 AWG 304 stainless braid	NA
(C) S.S. White Bi-directional hollow shaft coil	067N133C	Stainless Steel	NA	In-house polyurethane

The final results of all testing showed that candidate B was the most compatible for the prototype. The tubing could withstand rotation at 20,000 RPM in the tortuous loop and also provided the largest inner diameter to reduce resistance against sweep gas flow.

A.1 EFFECT OF FLUID VISCOSITY ON TORQUE

The test was performed in a straight test section to evaluate whether fluid viscosity would have a noticeable effect on torque transmission. This was done to ensure that testing in water was suitable and that an increase in viscosity to that of blood would not add excessive torque to the motor or tubing that should be considered. The test was performed using tubing sample A in both water and air. Figure A-1 shows that fluid viscosity had a negligible effect in our applicable ranges.

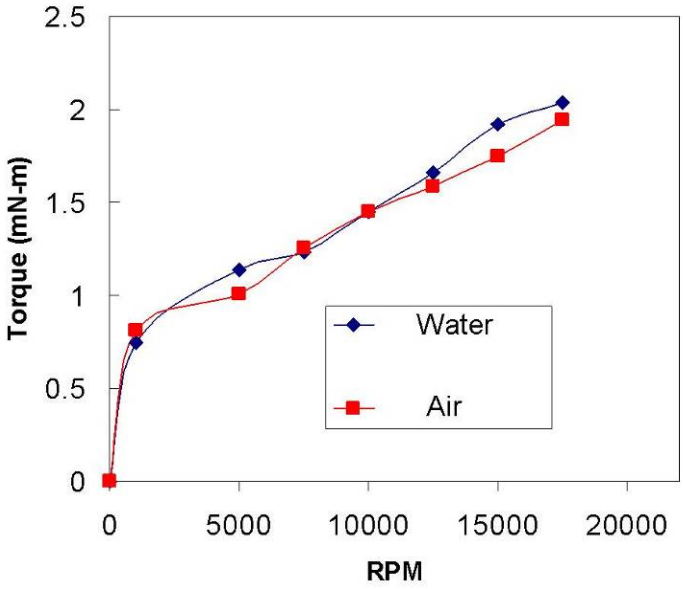

Figure A-1: Fluid viscosity influence on required motor torque.

A.2 IMPELLER UNIT LENGTH

All impeller units were fabricated from rigid materials and thus constrained tubing flexbility. Fixing the units to the impeller tubing required both a unit length and spacing to be determined. The spacing between units was arbitrarily set at 0.5". Sample C was tested in the loop with two impeller configurations consisting of either 1" impeller units or 0.5" impeller units. The test was conducted at 20,000 RPM and 1" units were concluded to provide inadequate flexibility. The longer units constrained the tubing to greater bending stresses in between units. Figure A-2 displays pictures of the tortuous test section and 1" failure.

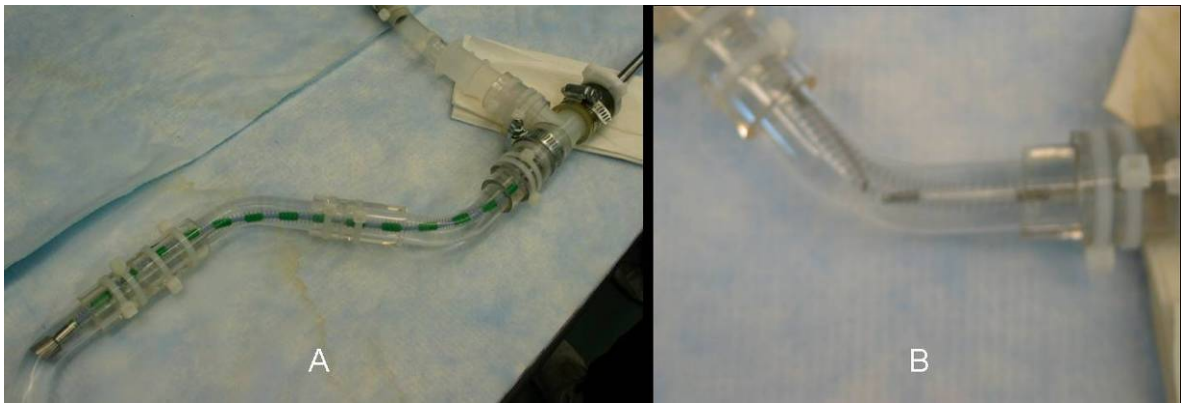

Figure A-2: (A) Tortuous test section. (B) Tubing break with 1" impeller units.

A.3 FATIGUE AND TORQUE REQUIREMENT

Test devices were placed in the tortuous configuration and operated at 20,000 RPM for fatigue life. Elapsed time and motor torque were monitored. A HFM bundle was also added to the N98-TOL-664 tubing test device to observe the effects on torque as bending radii decreased. Torque versus RPM results for tubing samples A and B are shown in Figure A-3. Both samples ran for over 6 hours without failure and were deemed useable in the prototype. The samples performed similarly in regards to torque requirement in the loop and the HFM bundle was observed to increase motor torque by an insignificant 0.5-1 mN-m. The recommended continuous torque application for the brushless servomoter was 13.5 mN-m and thus torque required in the “worst-case” scenario tortuous loop was still 3 times lower indicating motor-prototype compatibility.

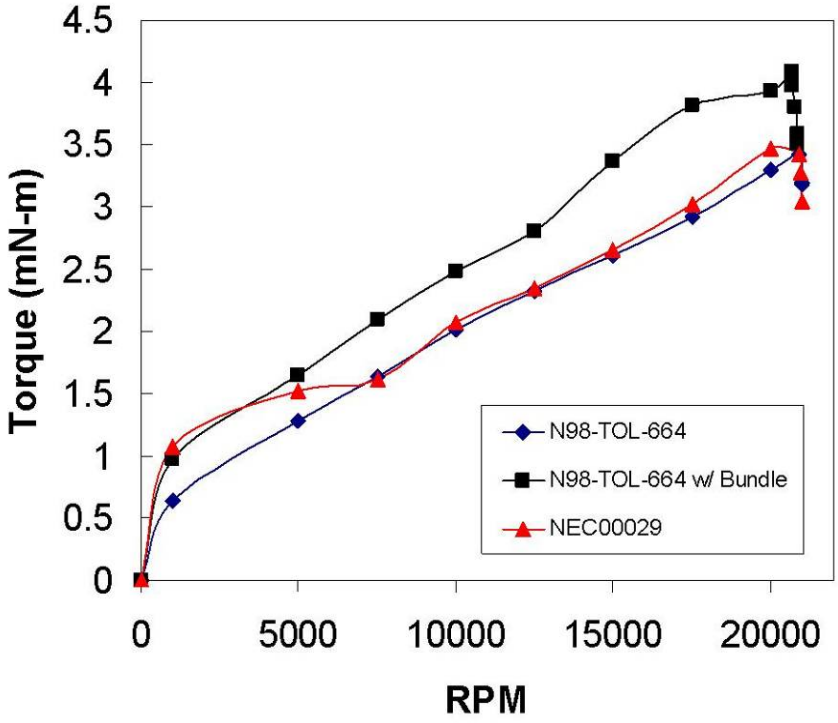

Figure A-3: Torque levels of tubing samples in tortuous configuration.

APPENDIX B

IMPELLER CATHETER DESIGN CALCULATIONS

The following calculations below were used in designing the impeller prototype. The blood shear stress calculation indicated a plausible cause for the build-up observed in the external bearings during *in vivo* testing. The saline purge calculation was used to meet the design requirement of 200 mmHg gauge pressure at the seal interface.

B.1 BLOOD SHEAR STRESS CALCULATION

Shear stress calculation for fully-developed, steady flow between concentric cylinders with outer cylinder fixed ($\omega_2=0$)[55]:

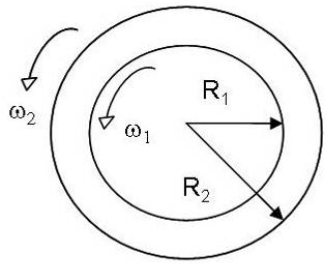

Figure B-1: Concentric rotating cylinders.

Laminar Flow $(\mathrm{Re} < 1700)$ between Rotating Cylinders when $\omega_2 = 0$:

$$\mathrm{Re} = \omega_1 R_1 \frac{\delta}{\nu} \qquad \text{where } \delta = R_2 - R_1$$

Shear stress τ_1, on the inner cylinder is:

$$\tau_{r\theta} = -\left[\mu r \frac{d}{dr}\left(\frac{V_\theta}{r}\right)\right]_{r = R_1} \quad \text{where } V_\theta = \frac{R_1^2 \omega_1}{R_2^2 - R_1^2}\left(\frac{R_2^2}{r} - r\right)$$

$$\therefore \tau_{r\theta} = \frac{2\mu R_2^2 \omega_1}{R_2^2 - R_1^1}$$

Calculation for impeller rotation at 20,000 RPM:

$$\omega_1 = 20{,}000 \bullet \frac{2\pi \text{ rad}}{60 \text{ s}} = 2094 \frac{\text{rad}}{\text{s}}$$

$\mu_{blood} = 0.033 \text{ P}$

$\nu_{blood} = 0.031 \frac{cm^2}{s}$

$R_1 = 0.142 \text{ cm}$

$R_2 = 0.144 \text{ cm}$

At 20,000 RPM,

$\mathrm{Re} = 19.2 < 1700 \ \therefore$ flow is laminar

$$\boxed{\tau_{r\theta} = 5010 \frac{dyne}{cm^2}}$$

B.2 SALINE PURGE FLOWRATE CALCULATION

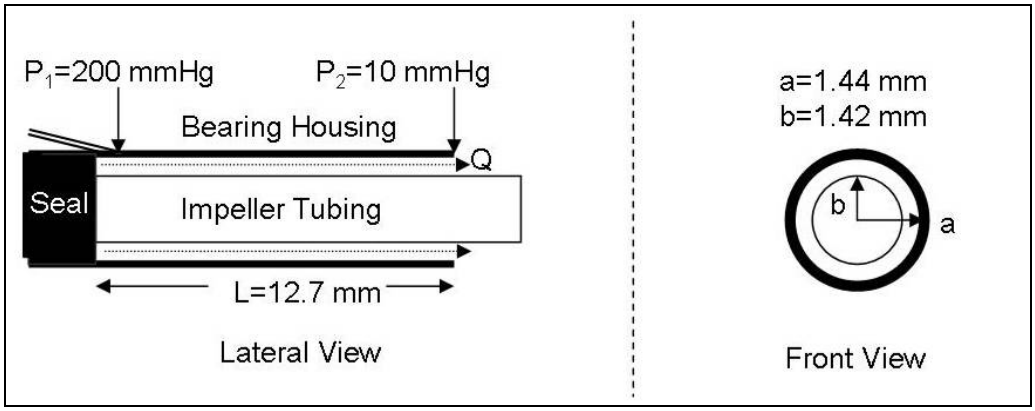

Figure B-2: Impeller catheter external bearing schematic.

Flow through an annulus is calculated according to[56]:

$$Q = \frac{\pi}{8\mu}\left(-\frac{dP}{dx}\right)\left[a^4 - b^4 - \frac{\left(a^2 - b^2\right)^2}{\ln(a/b)}\right]$$

Assume linear pressure gradient :

$$-\frac{dP}{dx} = \frac{P_2 - P_1}{L}$$

$P_1 = 26{,}664\ \text{Pa}$

$P_2 = 1{,}333\ \text{Pa}$

$\mu = 0.001\ \text{Pa - s}$

$L = 0.0127\ \text{m}$

$a = 0.001435\ \text{m}$

$b = 0.001422\ \text{m}$

$$Q = 3.28\ \text{x}10^{-9}\ \frac{\text{m}^3}{s} = 12\ \frac{\text{ml}}{\text{hr}}$$

APPENDIX C

C.1 IMPELLER PROTOTYPE *IN VIVO* PROTOCOL

Impeller Catheter Acute *In vivo* Test Protocol

February 27, 2007

Purpose: **To evaluate the impeller catheter in a calf model for gas exchange and hemodynamics at various rotation rates. To compare gas exchange results to *in vitro* water data.**

Devices:
1. Impeller: Vadnais coil tubing with Pebax heat-shrink/ 4-flat impeller units/ saline purge
2. Impeller: Vadnais coil tubing with Pebax heat-shrink/ RAX impeller units/ saline purge
3. Impeller: Vadnais coil tubing with Pebax heat-shrink/ sawtooth impeller units/ saline purge

PROTOCOL:

Night Before Preparation:

1) Calibrate all equipment (Gas Flowmeter, Pressure Transducer)
2) Setup equipment and make albumin soaking solution and heparinized saline (0.02 v/v)

Day of Test:

1) Calibrate CO_2 analyzer.
2) Soak device in albumin/heparin solution. (50cc bovine albumin, 10cc heparin, and saline)
3) Fill moisture trap container with ice.
4) Take baseline blood samples.
5) Insert all necessary pressure lines and take baseline measurements (CO, pressures):
   - **Left femoral vein**
   - **Carotid artery**
   - **Swan-Ganz – CVP and CO**
6) Measure diameter of right external jugular vein once exposed.
7) Measure initial hematocrit and CO, then begin volume loading with lactated ringers at 15ml/kg. After volume loading, measure hematocrit and CO again.
8) The magnetic guide system will be inserted via the **right femoral vein** and **right external jugular vein**, using Fluoroscopy.
9) Pull wires back and attach distal tip of catheter to femoral guide wire.
10) Allow 2 minutes for saline flush of device to initiate.
11) Administer a **heparin bolus** through the **left femoral line**.
12) Insert the catheter into the **right jugular with animal positioned on its side**.
13) Pull catheter through the jugular vein and position spanning the RA. Verify with Fluoroscopy.
14) Set the **gas flow to maximum allowed** and begin rotating at 5000 RPM. A post-insertion CO and several gas exchange values should be acquired during the equilibrium phase. .
15) When exchange stabilizes, rotation rate protocol will begin.
16) Test the following rotation rates in a random order: 5000, 10000, 15000, 20000 RPM, repeating each point twice. **Record $\%CO_2$, rotation rate, current, gas flow rate, and gas pressure drop.**
17) Reduce the rotation rate and record 200 RPM exchange rate. Obtain a CO at 200 RPM.
18) When finished with all rotation rates, move the device into **the IVC**.
19) Allow ~15 minute stabilization period with rotation at 5000 RPM. Take another CO.
20) Repeat steps 18-19 in this new location.
21) Remove device and place additional impeller devices. Repeat steps 13-21.
22) Keep the device in the second location for necropsy.
23) Pictures and anatomic measurements will be taken at necropsy.
24) Perform gross examination of organs (lung especially) and send out for histology samples if needed.

C.2 *IN VIVO* HEMOLYSIS GENERATION

Figure C-1 displays measured PFHB during all *in vivo* testing of the impeller prototype. Each color represents a separate calve experiment. The duration of testing time and goal of measuring efficiency for three impeller geometries per calve were not conducive to drawing conclusions about IP-2 hemolysis generation. PFHB ranged between 20-40 mg/dL for each animal during prototype testing. The trends indicated PFHB levels remaining constant or beginning to decrease over the course of testing but the effect of impeller rotation, rotation rate, and geometry could not be concluded.

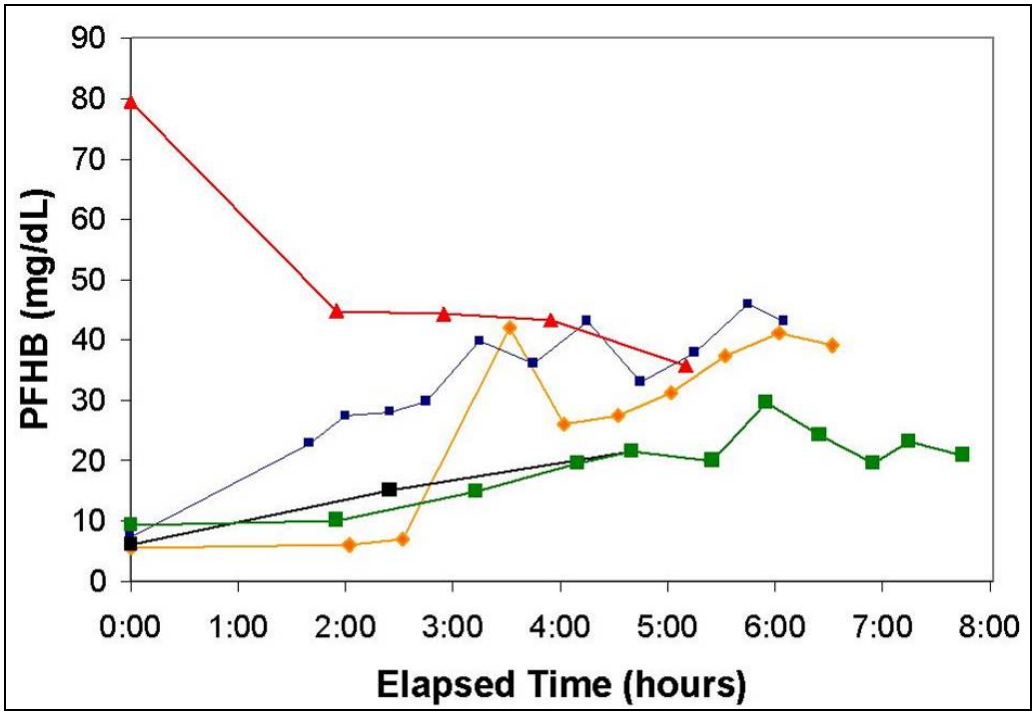

Figure C-1: IP-2 hemolysis generation in all animal implant studies.

BIBLIOGRAPHY

1. Diseases A to Z. http://www.lungusa.org/site/pp.asp?c=dvLUK9O0E&b=33316. American Lung Association. 2007 (accessed 1/4/2007).

2. Barnes PJ: Therapy of chronic obstructive pulmonary disease. *Pharmacol Ther* 97: 87-94, 2003.

3. Bernard GR, Artigas A, Brigham KL*, et al:*: Report of the American-European consensus conference on ARDS: definitions, mechanisms, relevant outcomes and clinical trial coordination. The Consensus Committee. *Intensive Care Med* 20: 225-232, 1994.

4. Hemmila MR, Napolitano LM: Severe respiratory failure: advanced treatment options. *Crit Care Med* 34: S278-290, 2006.

5. Frutos-Vivar F, Ferguson ND, Esteban A: Epidemiology of acute lung injury and acute respiratory distress syndrome. *Semin Respir Crit Care Med* 27: 327-336, 2006.

6. Bauldoff GS, Diaz PT: Improving outcomes for COPD patients. *Nurse Pract* 31: 26-28, 33-43; quiz 43-25, 2006.

7. Chronic Obstructive Pulmonary Disease Data Fact Sheet. http://www.nhlbi.nih.gov/health/public/lung/other/copd_fact.htm. National Institute of Health. 2003 (accessed 1/4/2007).

8. Levitt JE, Matthay MA: Treatment of acute lung injury: historical perspective and potential future therapies. *Semin Respir Crit Care Med* 27: 426-437, 2006.

9. Adhikari N, Burns KE, Meade MO: Pharmacologic treatments for acute respiratory distress syndrome and acute lung injury: systematic review and meta-analysis. *Treat Respir Med* 3: 307-328, 2004.

10. Delong P, Murray JA, Cook CK: Mechanical ventilation in the management of acute respiratory distress syndrome. *Semin Dial* 19: 517-524, 2006.

11. Ramnath VR, Hess DR, Thompson BT: Conventional mechanical ventilation in acute lung injury and acute respiratory distress syndrome. *Clin Chest Med* 27: 601-613; abstract viii, 2006.

12. Tremblay LN, Slutsky AS: Ventilator-induced lung injury: from the bench to the bedside. *Intensive Care Med* 32: 24-33, 2006.

13. Bartlett RH: Extracorporeal life support in the management of severe respiratory failure. *Clin Chest Med* 21: 555-561, 2000.

14. Conrad SA, Zwischenberger JB, Grier LR, Alpard SK, Bidani A: Total extracorporeal arteriovenous carbon dioxide removal in acute respiratory failure: a phase I clinical study. *Intensive Care Med* 27: 1340-1351, 2001.

15. Gay SE, Ankney N, Cochran JB, Highland KB: Critical care challenges in the adult ECMO patient. *Dimens Crit Care Nurs* 24: 157-162; quiz 163-154, 2005.

16. Rich PB, Rock P: Extracorporeal life support for severe adult respiratory failure. *Curr Opin Anaesthesiol* 16: 105-111, 2003.

17. Truskey GA, Yuan F, Katz DF (ed): *Transport phenomena in biological systems*. Upper Saddle River, N.J., Pearson/Prentice Hall, 2004.

18. Mortensen JD: An intravenacaval blood gas exchange (IVCBGE) device. A preliminary report. *ASAIO Trans* 33: 570-573, 1987.

19. Mortensen JD, Berry G: Conceptual and design features of a practical, clinically effective intravenous mechanical blood oxygen/carbon dioxide exchange device (IVOX). *Int J Artif Organs* 12: 384-389, 1989.

20. Mortensen JD: Intravascular oxygenator: a new alternative method for augmenting blood gas transfer in patients with acute respiratory failure. *Artif Organs* 16: 75-82, 1992.

21. Ventilation with lower tidal volumes as compared with traditional tidal volumes for acute lung injury and the acute respiratory distress syndrome. The Acute Respiratory Distress Syndrome Network. *N Engl J Med* 342: 1301-1308, 2000.

22. Brunet F, Mira JP, Cerf C, *et al:*: Permissive hypercapnia and intravascular oxygenator in the treatment of patients with ARDS. *Artif Organs* 18: 826-832, 1994.

23. Hattler BG, Federspiel WJ: Gas exchange in the venous system : Support for the failing lung, in Vaslef SN, Anderson RW (ed), *The Artificial Lung*, Georgetown, TX, Landes Bioscience, 2002, pp. 133-174.

24. Conrad SA, Eggerstedt JM, Grier LR, Morris VF, Romero MD: Intravenacaval membrane oxygenation and carbon dioxide removal in severe acute respiratory failure. *Chest* 107: 1689-1697, 1995.

25. Conrad SA, Bagley A, Bagley B, Schaap RN: Major findings from the clinical trials of the intravascular oxygenator. *Artif Organs* 18: 846-863, 1994.

26. Tao W, Schroeder T, Bidani A, *et al:*: Improved gas exchange performance of the intravascular oxygenator by active blood mixing. *Asaio J* 40: M527-532, 1994.

27. Federspiel WJ, Hout MS, Hewitt TJ, *et al:*: Development of a low flow resistance intravenous oxygenator. *Asaio J* 43: M725-730, 1997.

28. Federspiel WJ, Svitek RG: Artificial lungs: Current research and future directions., in Wnek GE, Bowlin GL (ed), *Encyclopedia of biomaterials and biomedical engineering*, New York, NY, Marcel Dekker, Inc., 2004, pp. 922-931.

29. Federspiel WJ, Golob JF, Merrill TL, *et al:*: Ex vivo testing of the intravenous membrane oxygenator. *Asaio J* 46: 261-267, 2000.

30. Tao W, Zwischenberger JB, Nguyen TT, *et al:*: Performance of an intravenous gas exchanger (IVOX) in a venovenous bypass circuit. *Ann Thorac Surg* 57: 1484-1490; discussion 1490-1481, 1994.

31. Eash HJ, Frankowski BJ, Litwak K, Wagner WR, Hattler BG, Federspiel WJ: Acute in vivo testing of a respiratory assist catheter: implants in calves versus sheep. *Asaio J* 49: 370-377, 2003.

32. Eash HJ, Budilarto SG, Hattler BG, Federspiel WJ: Investigating the effects of random balloon pulsation on gas exchange in a respiratory assist catheter. *Asaio J* 52: 192-195, 2006.

33. Snider MT, High KM, Richard RB, *et al:*: Small intrapulmonary artery lung prototypes: design, construction, and in vitro water testing. *Asaio J* 40: M533-539, 1994.

34. Nodelman V, Baskaran H, Ultman JS: Enhancement of O2 and CO2 transfer through microporous hollow fibers by pressure cycling. *Ann Biomed Eng* 26: 1044-1054, 1998.

35. High KM, Nicholson T, Richard RB, Panol GR, Shelley K, Snider MT: Effects of blood phase oscillation on gas transfer in a microporous intravascular lung. *Asaio J* 40: M735-739, 1994.

36. Vaslef SN, Mockros LF, Anderson RW: Development of an intravascular lung assist device. *ASAIO Trans* 35: 660-664, 1989.

37. Makarewicz AJ, Mockros LF, Anderson RW: A pumping intravascular artificial lung with active mixing. *Asaio J* 39: M466-469, 1993.

38. Makarewicz AJ, Mockros LF, Anderson RW: A dynamic intravascular artificial lung. *Asaio J* 40: M747-750, 1994.

39. Cattaneo G, Strauss A, Reul H: Compact intra- and extracorporeal oxygenator developments. *Perfusion* 19: 251-255, 2004.

40. Cattaneo GF, Reul H: New fiber configuration for intravenous gas exchange. *Int J Artif Organs* 28: 244-250, 2005.

41. Cattaneo GF, Reul H, Schmitz-Rode T, Steinseifer U: Intravascular blood oxygenation using hollow fibers in a disk-shaped configuration: experimental evaluation of the relationship between porosity and performance. *Asaio J* 52: 180-185, 2006.

42. Federspiel WJ, Hattler BG: Sweep gas flowrate and CO2 exchange in artificial lungs. *Artif Organs* 20: 1050-1052, 1996.

43. Eash HJ, Frankowski BJ, Hattler BG, Federspiel WJ: Evaluation of local gas exchange in a pulsating respiratory support catheter. *Asaio J* 51: 152-157, 2005.

44. Eash HJ, Mihelc KM, Frankowski BJ, Hattler BG, Federspiel WJ: Evaluation of fiber bundle rotation for enhancing gas exchange in a respiratory assist catheter. *Asaio J* 53: 368-373, 2007.

45. Lund LW, Hattler BG, Federspiel WJ: A comparative in vitro hemolysis study of a pulsating intravenous artificial lung. *Asaio J* 48: 631-635, 2002.

46. Kameneva MV, Antaki JF, Yeleswarapu KK, Watach MJ, Griffith BP, Borovetz HS: Plasma protective effect on red blood cells exposed to mechanical stress. *Asaio J* 43: M571-575, 1997.

47. Svitek RG, Frankowski BJ, Federspiel WJ: Evaluation of a pumping assist lung that uses a rotating fiber bundle. *Asaio J* 51: 773-780, 2005.

48. White FM: Turbomachinery, in (ed), *Fluid Mechanics*, New York, McGraw-Hill, 1998, pp. 711-813.

49. Reich S and Gates WH: Centrifugal blood pump for cardiac assist. USA Patent 1979.

50. Federspiel WJ, Hewitt T, Hout MS*, et al:*: Recent progress in engineering the Pittsburgh intravenous membrane oxygenator. *Asaio J* 42: M435-442, 1996.

51. Vaslef SN, Mockros LF, Anderson RW, Leonard RJ: Use of a mathematical model to predict oxygen transfer rates in hollow fiber membrane oxygenators. *Asaio J* 40: 990-996, 1994.

52. Vaslef SN, Mockros LF, Cook KE, Leonard RJ, Sung JC, Anderson RW: Computer-assisted design of an implantable, intrathoracic artificial lung. *Artif Organs* 18: 813-817, 1994.

53. Mockros LF, Leonard R: Compact cross-flow tubular oxygenators. *Trans Am Soc Artif Intern Organs* 31: 628-633, 1985.

54. Paul R, Apel J, Klaus S, Schugner F, Schwindke P, Reul H: Shear stress related blood damage in laminar couette flow. *Artif Organs* 27: 517-529, 2003.

55. Potter MCaW, David C. (ed): *Mechanics of Fluids* Upper Saddle River, Prentice Hall, 1997.

56. White FM: Solutions of the Newtonian Viscous-Flow Equations, in (ed), *Viscous Fluid Flow*, Boston, McGraw-Hill, 1991, pp. 104-211.